Multiple expressions of plume-ridge interaction in the Galápagos: Volcanic lineaments and ridge jumps

E. Mittelstaedt and S. Soule
Department of Geology and Geophysics, Woods Hole Oceanographic Institution, Woods Hole, Massachusetts 02543, USA (emittelstaedt@whoi.edu)

K. Harpp
Department of Geological Sciences, University of Idaho, Moscow, Idaho 83844, USA

D. Fornari
Department of Geology and Geophysics, Woods Hole Oceanographic Institution, Woods Hole, Massachusetts 02543, USA

C. McKee
Department of Geology, Colgate University, Hamilton, New York 13346, USA

M. Tivey
Department of Geology and Geophysics, Woods Hole Oceanographic Institution, Woods Hole, Massachusetts 02543, USA

D. Geist
Department of Geological Sciences, University of Idaho, Moscow, Idaho 83844, USA

M. D. Kurz
Department of Geology and Geophysics, Woods Hole Oceanographic Institution, Woods Hole, Massachusetts 02543, USA

C. Sinton
Department of Environmental Studies and Sciences, Ithaca College, Ithaca, New York 14850, USA

C. Mello
Department of Geology, Colgate University, Hamilton, New York 13346, USA

[1] Anomalous volcanism and tectonics between near-ridge mantle plumes and mid-ocean ridges provide important insights into the mechanics of plume-lithosphere interaction. We present new observations and analysis of multibeam, side scan sonar, sub-bottom chirp, and total magnetic field data collected during the R/V Melville FLAMINGO cruise (MV1007; May–June, 2010) to the Northern Galápagos Volcanic Province (NGVP), the region between the Galápagos Archipelago and the Galápagos Spreading Center (GSC) on the Nazca Plate, and to the region east of the Galápagos Transform Fault (GTF) on the Cocos Plate. The NGVP exhibits pervasive off-axis volcanism related to the nearby Galápagos hot spot, which has dominated the tectonic evolution of the region. Observations indicate that ∼94% of the excess volcanism in our

survey area occurs on the Nazca Plate in three volcanic lineaments. Identified faults in the NGVP are consistent with normal ridge spreading except for those within a ~60 km wide swath of transform-oblique faults centered on the GTF. These transform-oblique faults are sub-parallel to the elongation direction of larger lineament volcanoes, suggesting that lineament formation is influenced by the lithospheric stress field. We evaluate current models for lineament formation using existing and new observations as well as numerical models of mantle upwelling and melting. The data support a model where the lithospheric stress field controls the location of volcanism along the lineaments while several processes likely supply melt to these eruptions. Synthetic magnetic models and an inversion for crustal magnetization are used to determine the tectonic history of the study area. Results are consistent with creation of the GTF by two southward ridge jumps, part of a series of jumps that have maintained a plume-ridge separation distance of 145 km to 215 km since ~5 Ma.

1. Introduction

[2] Mantle plumes dominate the tectonic and volcanic evolution of nearby ridge axes and the overlying lithosphere [e.g., *Ito et al.*, 2003]. Off-axis expressions of mantle plumes include the formation of oceanic islands with enriched trace element and isotopic ratios [e.g., *Harpp and White*, 2001] and large hot spot swells that can span hundreds of kilometers [*Schilling*, 1991]. Between the plume and ridge, observations reveal volcanic lineaments, propagating ridges, and abandoned spreading centers caused by ridge jumps, which alter the evolution of these plate boundaries [*Hey and Vogt*, 1977; *Morgan*, 1978; *Small*, 1995; *Wilson and Hey*, 1995] [e.g., *Hardarson et al.*, 1997; *Harpp and Geist*, 2002; *Harpp et al.*, 2003; *Mittelstaedt and Ito*, 2005; *Maia et al.*, 2011]. For example, repeated ridge jumps have effectively pinned the Reykjanes Ridge near the Iceland Plume since ~20 Ma, despite relative motion between the two [*Hardarson et al.*, 1997; *Garcia et al.*, 2003]. In the Galápagos, the plume has not only resulted in numerous jumps of the axis toward the hot spot [*Wilson and Hey*, 1995; *Meschede and Barckhausen*, 2000], but also voluminous off-axis volcanism that formed the Galápagos Archipelago

and a series of volcanic lineaments between the plume and the ridge [*Harpp and Geist*, 2002; *Harpp et al.*, 2003; *Geist et al.*, 2008]. The mechanisms controlling the formation of such off-axis lineaments as well as the initiation and evolution of ridge jumps are poorly understood.

[3] The Galápagos system is an ideal location to study plume-ridge interaction due to the well-known regional tectonic history, and the location, chemistry, and axial expressions of the Galápagos Plume [*White et al.*, 1993; *Wilson and Hey*, 1995; *Canales et al.*, 1997; *Kurz and Geist*, 1999; *Harpp and White*, 2001; *Canales et al.*, 2002; *Detrick et al.*, 2002; *Hooft et al.*, 2003; *Schilling et al.*, 2003; *Sinton et al.*, 2003; *Behn et al.*, 2004; *Blacic et al.*, 2004; *Cushman et al.*, 2004; *Christie et al.*, 2005; *O'Connor et al.*, 2007; *Villagómez et al.*, 2007; *Blacic et al.*, 2008; *Geist et al.*, 2008; *Kurz et al.*, 2009]. In particular, the region between the Galápagos Archipelago and the Galápagos Spreading Center (GSC) can provide insights into the more poorly studied off-axis manifestations of plume-ridge interaction. In this study, we use new shipboard data from the Galápagos region to examine the tectonic evolution and anomalous volcanism associated with this near-ridge hot spot.
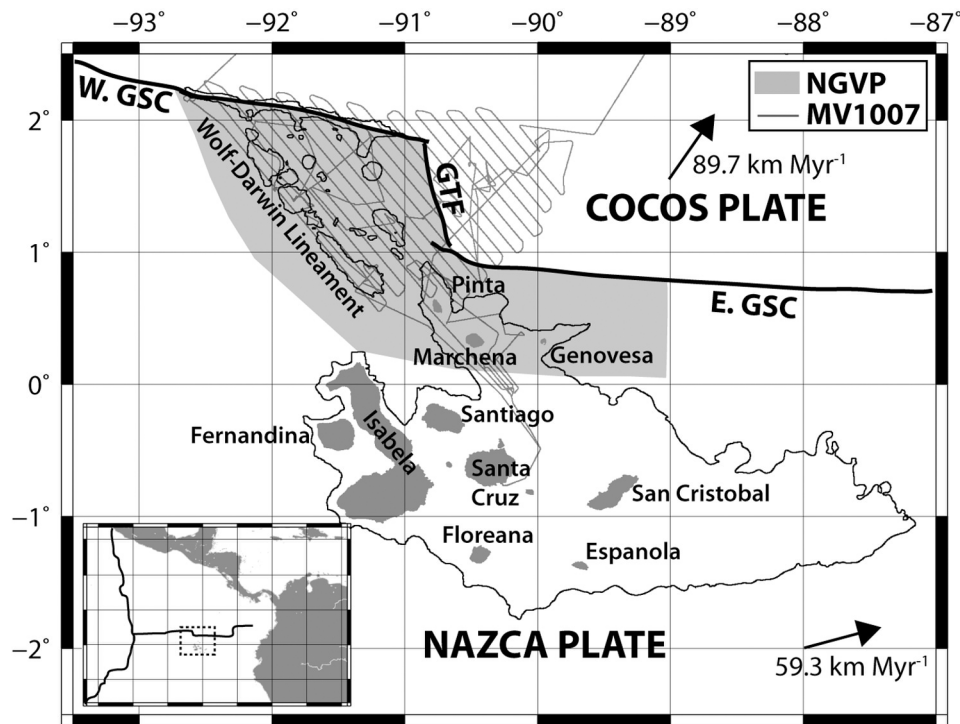
Figure 1. A simplified map of the Galápagos region with select contours (thin, black lines) based upon satellite-derived bathymetry [*Smith and Sandwell*, 1997] showing the location of major volcanic features. Contours are at depths of 1500 m around the archipelago and 1750 m around the lineaments. The FLAMINGO cruise collected underway geophysical data along tracks (gray lines) traversing the NGVP (gray area), north of the main Archipelago, and the region of the Cocos Plate east of the GTF. Nazca Plate motion of 59.3 km Myr^{-1} at an azimuth of 75° and Cocos Plate motion of 89.7 km Myr^{-1} at an azimuth of 35° are from the no-net-rotation reference frame model NNR_MORVEL56 [*Argus et al.*, 2011].

1.1. Plume-Ridge Interaction in the Galápagos

1.1.1. The Galápagos Archipelago

[4] The Galápagos Islands are located approximately 100 km–300 km south of the intermediate-spreading-rate Galápagos Spreading Center (GSC), which separates the Cocos Plate to the north from the Nazca Plate to the south (Figure 1). The archipelago lies at the convergence of the Cocos and Carnegie aseismic ridges, located on the Cocos and Nazca plates respectively. The islands rest atop a large volcanic platform that rises ~3000 m from the surrounding seafloor [*Geist et al.*, 2008]; part of the ~15 km thick crust above the hot spot [*Toomey et al.*, 2001]. The islands, aseismic ridges, and the volcanic platform are all expressions of the Galápagos hot spot that is presumed to be centered near Fernandina and Isabela Islands, the most volcanically active islands in the archipelago and the location of the greatest ^{3}He/^{4}He values detected in the archipelago [*Kurz and Geist*, 1999].

1.1.2. A Mantle Plume Beneath the Galápagos Islands

[5] Both geophysical and geochemical studies support the hypothesis that a chemically distinct, hot, mantle plume upwelling beneath the Galápagos Islands is the source of volcanism on the archipelago. Teleseismic receiver functions reveal a thinned transition zone beneath the southwestern part of the archipelago, consistent with localized, anomalously hot ($\Delta T \sim 150°C$) upwelling from the deep mantle (>400 km) [*Hooft et al.*, 2003]. At shallower depths (<150 km), there is a continuous zone of slow seismic velocities in the mantle beneath Cerro Azul and Fernandina volcanoes [*Villagómez et al.*, 2007]. This slow velocity anomaly extends to the northeast and west toward the GSC, broadening as it shoals beneath a high velocity lid. *Villagómez et al.* [2007] interpret the velocity anomaly to reflect spreading of sub-lithospheric plume material.

1.1.3. Plume-Ridge Interaction Along the Galápagos Spreading Center

[6] *Schilling et al.* [1982] identify a well-defined, long-wavelength, symmetrical pattern of increasing plume contribution to axial lavas along the GSC as it nears the Galápagos Archipelago. This pattern is manifest in enriched radiogenic isotope ratios (Pb, Sr, Hf, Nd) and incompatible element ratios (e.g., K/Ti; La/Yb) [*Verma and Schilling*, 1982; *Verma*, 1983; *Detrick et al.*, 2002; *Schilling et al.*, 2003; *Cushman et al.*, 2004; *Christie et al.*, 2005; *Kokfelt et al.*, 2005] and is continuous in axial lavas across the 90.5°W Galápagos Transform Fault (GTF) [*Schilling et al.*, 1982, 2003; *Christie et al.*, 2005].

[7] Geophysical and morphological observations are also consistent with extensive plume-ridge interaction along the GSC. The ridge shoals by approximately 1 km within ~600 km east and west of the hot spot, develops an axial high morphology typical of fast spreading ridges despite its intermediate spreading rate, and has up to a ~60 mGal negative mantle Bouguer anomaly [*Ito and Lin*, 1995; *Canales et al.*, 1997, 2002; *Christie et al.*, 2005]. Along the Western GSC, approximately half the swell amplitude and the gravity anomaly are caused by as much as 2.3 km of excess crust [*Canales et al.*, 2002], while the remaining contributions are attributed to thermal ($\Delta T \sim 30°C$ at the GSC) and compositional anomalies in the underlying mantle [*Ito and Lin*, 1995; *Canales et al.*, 2002].

[8] Magnetic anomaly modeling reveals that ridge jumps toward the plume have maintained a small plume-ridge separation distance while the entire GSC migrated northeastward since ~10 Ma [*Hey*, 1977; *Wilson and Hey*, 1995]. V-shaped discontinuities in the anomaly pattern indicate that most new ridge segments propagate at rates of 30 km Myr^{-1} to 120 km Myr^{-1} away from the hot spot subsequent to southward jumps of the axis [*Wilson and Hey*, 1995]. In part due to these repeat jumps of the axis, oceanic crust created along the GSC in the last ~10 Myr preferentially accreted onto the Cocos Plate to the north [*Wilson and Hey*, 1995].

1.2. Off-Axis Manifestations of the Galapagos Hot Spot

1.2.1. The Northern Galápagos Volcanic Province

[9] Located between the Galápagos Archipelago and the GSC, between ~92°30′W and ~89°W, the Northern Galápagos Volcanic Province (NGVP) includes five emergent islands (Wolf, Darwin, Pinta, Marchena, and Genovesa) and several volcanic lineaments arrayed in a fan-shaped pattern (Figures 1 and 2) [*Morgan*, 1978; *Harpp and Geist*, 2002; *Harpp et al.*, 2003; *Sinton et al.*, 2003]. The few existing $^{40}Ar/^{39}Ar$ dates from dredges of the Wolf-Darwin Lineament (WDL) [*Sinton et al.*, 1996] and K-Ar dates from Wolf Island [*White et al.*, 1993] suggest that the lineaments formed within the last ~2 Myr. Unlike typical near-ridge seamounts, many of the largest seamounts and islands in the NGVP have notably elongate morphologies suggesting a structural influence in their development [*Batiza and Niu*, 1992; *Smith and Cann*, 1992; *Harpp and Geist*, 2002]. Even Genovesa Island, which has a nearly circular subaerial outline, is merely the emergent peak of a >60 km long, ridge-like seamount [*Harpp and Geist*, 2002; *Harpp et al.*, 2003]. Several studies have investigated the origin of the largest of these lineaments, the Wolf-Darwin Lineament (WDL, Figure 1), but sparse data have made it difficult to constrain the various models.

1.2.2. Current Models of Lineament Formation in the NGVP

[10] Models explaining the formation of the Galápagos lineaments fall into three categories: (1) magmatism driven by mantle dynamics; (2) magmatism controlled by large lithospheric-scale faults; and (3) magmatism controlled by deviatoric stresses in the lithosphere.

[11] *Morgan* [1978] initially attributed the Wolf-Darwin Lineament to a thermally eroded channel transporting material from the plume to the ridge. This model predicts seamount formation where this channel meets the ridge axis and an increase in seamount age away from the axis in accord with the seafloor age. The trend of these seamounts is predicted to be along the vector subtraction of absolute plate motion and the motion of the GSC away from the hot spot. Similarly, *Small* [1995] explains volcanic lineaments at near-ridge hot spots, including the WDL, as the result of asymmetric spreading along the ridge induced by elevated temperatures and excess magmatism associated with the plume. *Small* [1995] also notes that gravity lineations exist between ridges and hot spots globally and suggests they reflect asthenospheric flux from the plume to the ridge along the base of the lithosphere.
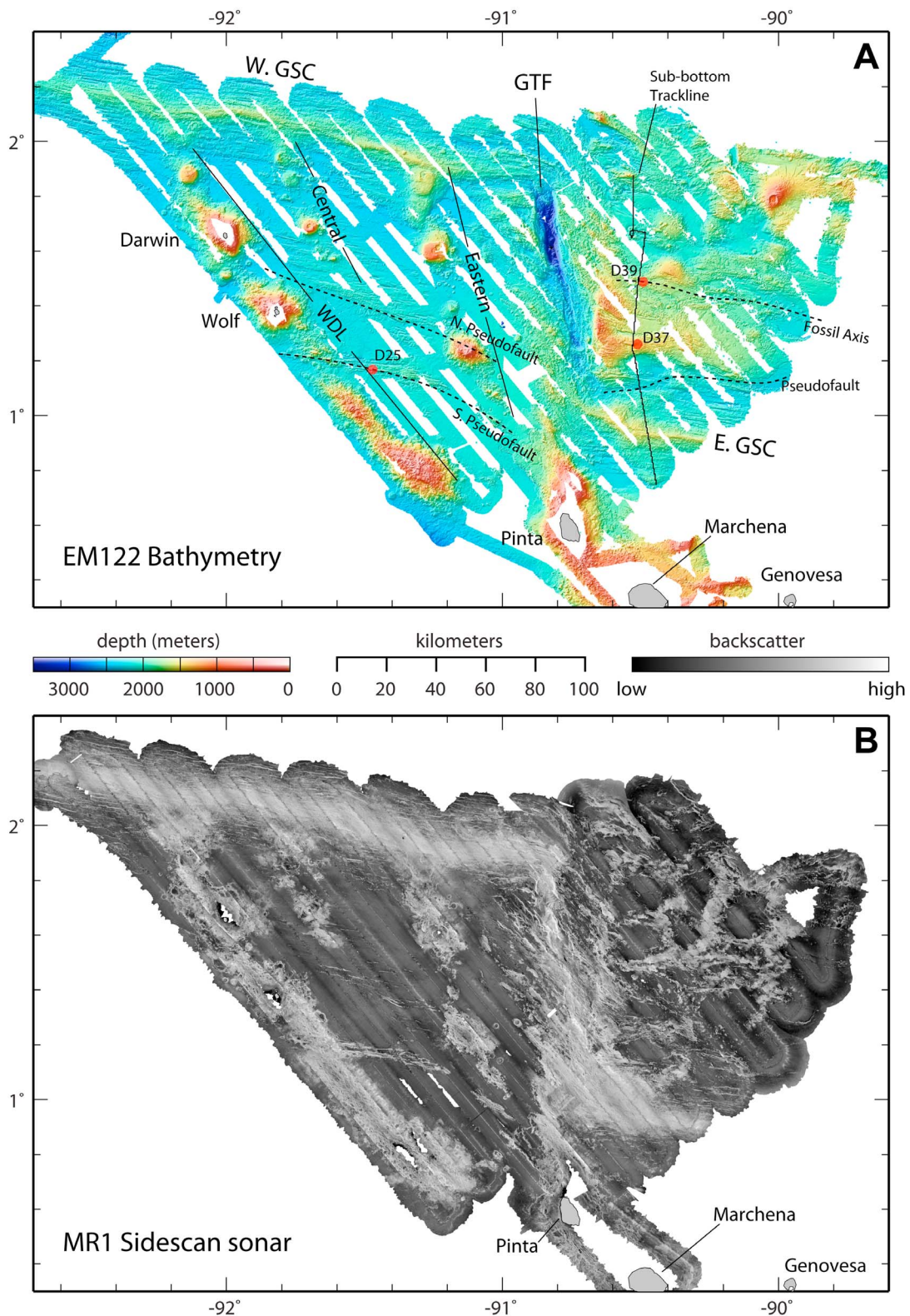
Figure 2. Multibeam bathymetry and side scan sonar reflectivity collected in the NGVP and east of the GTF during the FLAMINGO cruise (MV1007, May–June 2010). (a) Bathymetry were collected using a hull-mounted EM-122 system and gridded at 50 m resolution. Bathymetric features of interest are as labeled. Red circles denote locations where three dredges of highly differentiated lavas were collected (section 3.6). (b) Reflectivity data were collected with the HMRG MR-1 near-surface towed sonar system and gridded at 8 m resolution.

[12] On the basis of gravity modeling, *Feighner and Richards* [1994] suggested that the Wolf-Darwin Lineament (WDL) lies along a lithospheric-scale fault defining a boundary between Airy compensated lithosphere northeast of the WDL and a thick elastic plate to its southwest. Possible mechanisms for the discontinuity in lithospheric thickness include the age offset generated by the GTF, contrasts in lithospheric age across pseudofaults, and thermal erosion of the lithosphere by the plume. Although the modeling of *Feighner and Richards* [1994] does not specifically address lineaments other than the WDL, it is reasonable to assume that processes controlling the creation of the WDL would be similar to those responsible for the other lineaments in the NGVP and at other hot spots. The specific source of the melts that form the lineament volcanoes is not addressed in this model.

[13] The final class of models suggests that the locations and orientations of the Galápagos lineaments are controlled by the regional stress field of the Nazca plate. Using a compilation of existing bathymetry and geochemical data, *Harpp and Geist* [2002] and *Harpp et al.* [2003] proposed that the lineament orientations result from perturbations to the lithospheric stress field associated with friction along the GTF [e.g., *Gudmundsson*, 1995] and extension due to oblique slip along the GTF [e.g., *Taylor et al.*, 1994]. Magma in these models is assumed to derive from excess melting associated with the nearby hot spot. Alternatively, *Sinton et al.* [2003] posited that the lineament pattern is an expression of the lithospheric stress field resulting from the mantle plume impinging on the base of the plate at the northern edge of the Galápagos platform.

[14] *Mittelstaedt and Ito* [2005] applied thin-plate theory to calculate the two-dimensional pattern of depth-integrated stresses in near-ridge lithosphere associated with the ridge-transform-ridge boundary, and with buoyant uplift and asthenospheric shear of a radially spreading mantle plume. Assuming that the lineaments act as cracks and lengthen in the direction parallel to least tensile stress, these calculations reproduce a similar fan-shaped pattern to the Galápagos lineaments. However, unlike the model of *Harpp and Geist* [2002] that requires no specific age progression along the lineaments, *Mittelstaedt and Ito* [2005] predict the lineaments to initiate near the ridge axis, where the maximum tensile stress is estimated to be approximately equal to the lithospheric yield stress, and to propagate away from this initial location. Alternatively, the lineaments may initiate at pre-existing weaknesses in the plate related to ridge jumps and ridge propagations [*Villagómez et al.*, 2011].

[15] Here, we present analysis of new multibeam bathymetry, side scan sonar, total magnetic field, and sub-bottom chirp data of the NGVP on the Nazca Plate and the region directly east of the GTF on the Cocos Plate. These new data allow us to observe and quantify past and present manifestations of plume-lithosphere interaction on seafloor both overlying and on the far side of the ridge axis from the upwelling Galápagos mantle plume. Using these new data, simulations of mantle flow and melting, and data from previous studies, we evaluate the above models for formation of the volcanic lineaments in the NGVP. In addition, we present a new reconstruction of the evolution of the GSC between 92.5°W and 89°W, which includes previously unidentified southward ridge jumps both east and west of the GTF. Development of the GTF appears to have occurred in response to these jumps in two stages and is a direct consequence of plume-ridge interaction.

2. Data

2.1. Multibeam Bathymetry and Side Scan Sonar

[16] Sonar surveys were conducted along >5000 km of trackline, with tracks oriented at ~140° and separated by ~9.5 km (Figure 1). Multibeam bathymetry data were collected by a hull-mounted EM122 12 kHz sonar. Data were manually edited for spurious soundings and gridded at 50 m horizontal resolution (Figure 2a). Typical swath widths for the EM122 were 5–7 km resulting in 95% bathymetric coverage in the study area. Side scan sonar backscatter data were collected by the 11/12 kHz HMRG MR1 near-surface towed sonar system. The MR1 was operated on a slave pulse from the EM-122 to avoid interference between the two systems, yielding a swath width of ~11 km. The towfish was navigated by layback based on ship speed and wire out and processed swaths were merged to produce an 8-m-resolution acoustic backscatter mosaic with complete coverage over the survey area (Figure 2b). Both data sets are available through the Marine Geoscience Data System (www.mgds.org).

[17] Multibeam bathymetry and side scan sonar data are interpreted to identify the distribution of seamounts and faults. We employ two methods to map seamounts, manual digitization of bathymetric

Table 1. Included Magnetic Data[a]

Year	Research Vessel	Chief Scientist	Cruise Name	Cruise Number
1966	Robert D. Conrad	R. Wall	-	RC1004
1969	Yaquina	D. Heinrichs	Long Ocean - leg 4	YAQ69FEB
1972	Noroit	-	-	72001831
1973	Yaquina	G. Ross Heath	Long Ocean - leg 3	YAQ7303
1979	Kana Keoki	R. Hey	-	KK78123004
1979	Kana Keoki	R. Hey / D. Hussong	-	KK78123006
1979	Kana Keoki	D. Hussong	-	KK78123007
1987	Moana Wave	K. MacDonald	Studies of the EPR	MW8710
1989	Thomas Washington	N. Pisias	Venture, leg 1	VNTR01WT
1990	Thomas Washington	C. Cox	Plume leg 1	PLUM01WT
1991	JOIDES Resolution	L. Mayer, N. Pisias, T. Janeck	Ocean Drilling Project, leg 138	ODP138JR
2010	Melville	K. Harpp	FLAMINGO	MV1007

[a]Dashes (-) indicate that the name of the chief scientist or cruise was not included in the NGDC data record.

highs and acoustic backscatter anomalies, and automatic detection from bathymetry on the basis of closed-contour methods described in the works of *Behn et al.* [2004] and *Bohnenstiehl et al.* [2012]. Seamounts detected automatically using bathymetry require a minimum of two closed contours at a 10 m contour interval, so a minimum relative height of ~25 m. Those that were identified manually have a minimum diameter of ~300 m, which is ~30x the grid spacing of the side scan data, but theoretically seamounts 100 m in diameter could be identified confidently. The automatic method was used to identify roughly one quarter of the seamounts. Although the less subjective automated method is preferred, manual identification was more effective owing to the incomplete bathymetric data.

[18] We mapped the orientation and length of faults in the NGVP using a combination of ship-based multibeam bathymetry and side scan sonar backscatter imagery. Faults in side scan sonar imagery are identified based on bright (facing) or dark (shadowed), linear backscatter features. The faults are digitized along the tops of the scarps. From near-bottom photographic transects, we find that faults with >15 m throw are detected in the side scan sonar data. Faults identified in side scan sonar data were confirmed, where possible, in bathymetry data. Some faults were not visible in side scan sonar imagery, especially those within acoustically bright areas (e.g., within the transform valley and at the ridge axis) or heavily sedimented areas, and were digitized solely on the basis of bathymetric data.

2.2. Magnetic Data

[19] A Marine Magnetics SeaSPY magnetometer was towed near the sea surface 300 m behind the

R/V Melville during the surveys. Total magnetic field data were corrected for the regional geomagnetic field by subtracting the 2010 International Geomagnetic Reference Field model [*International Association of Geomagnetism and Aeronomy*, 2005], for daily variations by subtracting the daily deviations recorded at the Huancayo magnetic observatory, and for the navigational shift of 300 m between the magnetometer and the ship GPS location. The surveys are supplemented with data from the National Geophysical Data Center (Table 1) that were corrected with interpolated values of the Definitive Geomagnetic Reference Field corresponding to the year of their collection. The spacing of the compiled tracklines varies across the study from ~1 km to ~25 km with a mean spacing <10 km (insets, Figures 8a and 8b). Crossover analysis results in a mean crossover error of -5.7 nT with a standard deviation of the crossover misfits of 159.5 nT. Crossover data corrections [*Hsu*, 1995] performed using weights that decrease with age (i.e., more recent data are considered more accurate) result in a significant reduction of the misfit with final values of the mean crossover error of -0.95 nT and a standard deviation of the misfits of 25.3 nT. The compilation of magnetic data was smoothed and gridded at 250 m using the Generic Mapping Tools' blockmedian (1 km blocks) function followed by the greenspline function using a minimum curvature spline with a tension of 0.2 [*Wessel and Smith*, 1991]. The greenspline function uses a Green's function approach to solve for the coefficients of the chosen spline, yielding an exact interpolation of the supplied data points (www.soest.hawaii.edu/wessel/greenspline/).

[20] Following *Macdonald et al.* [1980], we use an extended form of the method of *Parker and Huestis* [1974] to perform a three-dimensional inversion of

the observed magnetic anomalies for the pattern of magnetization in a constant thickness layer (1 km) concordant with the seafloor bathymetry. The inversion removes the skewness due to latitude and corrects for variations in bathymetry. The magnitude of magnetization in the layer is assumed to vary only laterally and to have a constant direction parallel to that of the geomagnetic dipole (inclination = 2.7°). Inversion for the magnetization is approximately equivalent to a downward continuation of the magnetic anomalies and is inherently unstable. To ensure convergence of the solution, we use a cosine tapered bandpass filter with cutoff frequencies at 800 km and 2 km, a passband between 400 km and 4 km, and an azimuthal cutoff for $k_y/k_x < 0.9998$ (where k_y and k_x are orthogonal wave numbers) to avoid divergence of the solution near the equator. No magnetic annihilator is added to the magnetization solution. Recalculation of the magnetic field from the magnetization solution results in a root-mean square error of 52.3 nT over a total magnetic anomaly variation of >1500 nT.

[21] To aid in identification of magnetic anomalies in the resulting magnetization grid, we use a forward model to calculate synthetic ~N–S anomaly profiles. We use a Fourier method to calculate synthetic anomalies in a constant thickness source layer (1 km) with a uniform magnitude of magnetization [Parker and Huestis, 1974]. A synthetic history of seafloor magnetization is created by interpolating the geomagnetic timescale of Gradstein et al. [2004] to profiles of modeled seafloor age versus distance. Constraints applied to the model include the time over which a given spreading rate occurs, spreading rate, spreading asymmetry, and distance of any ridge jumps. As is commonly assumed [Hey, 1977; Wilson and Hey, 1995], ridge jumps are treated as instantaneous events because of the unconstrained duration of simultaneous spreading between two coexisting axes. This introduces unknown errors in the ages of jumps and overall spreading rates since axis transitions may last several hundreds of thousands to millions of years [Hardarson et al., 1997; Mittelstaedt et al., 2008, 2011]. Our final models are based upon best fits to anomaly patterns and corroborating geological observations.

2.3. Sub-bottom Chirp Data Processing

[22] We collected sub-bottom chirp data using a Knudsen 3.5 kHz echosounder along a trackline oriented parallel to the spreading direction and located east of the GTF (Figures 2a and 3). Data

processing is performed using the SIOSEIS processing software [Henkart, 1992]. We convert raw data to envelope data by taking the complex conjugate of the original signal and the Hilbert transform, or the analytic signal [Henkart, 2006]. A bandpass filter with frequency cutoffs at 2 Hz and 500 Hz, followed by a depth increasing gain function are then applied. Finally, the traces are hung at a constant time to create a flat seafloor and horizontal sediment packages. Sediment layers are identified as laterally continuous traces in the flattened sub-bottom data (Figure 3). The two-way travel times of the layers are converted to depth with a depth-dependent, linear sound velocity model between 1500 m/s to 1800 m/s in the top 150 m of the record. We estimate the error on the digitized sediment thicknesses as ±3 m.

3. Results

3.1. Volumes and Distribution of Volcanism

[23] To map individual seamounts within the NGVP, we use the newly collected multibeam bathymetry and side scan sonar data set that, due to improved resolution and coverage, allows us to resolve hundreds of previously undescribed seamounts (Figure 4). To the west of the GTF, the majority of the seamounts fall into three lineaments (n = 332), although numerous other isolated seamounts are observed throughout the area (n = 174). To the east of the transform, seamounts are randomly distributed and do not form any clear lineaments (n = 219).

[24] Seamount volumes are estimated by integrating bathymetric soundings within the seamount area relative to a plane fit to depth values around the seamount base (Figure 4 and Table 2). Seamounts that fall partially or completely outside of the gridded bathymetric data or edifices identified atop larger seamounts are excluded from this analysis. In addition, we determine maximum seamount height as well as seamount elongation and orientation by fitting an ellipse to the seamount boundary. The number of seamounts located west of the transform is more than two times greater than to the east, with the greatest number occurring within the Wolf-Darwin Lineament (n = 187). The volume of excess volcanism in the NGVP, as reflected in the seamounts, is significantly greater to the west of the transform (1178 km³), roughly 94% of the total seamount volume in our study area (Figure 4). Again, the WDL represents the greatest volume of seamount volcanism: 926 km³.
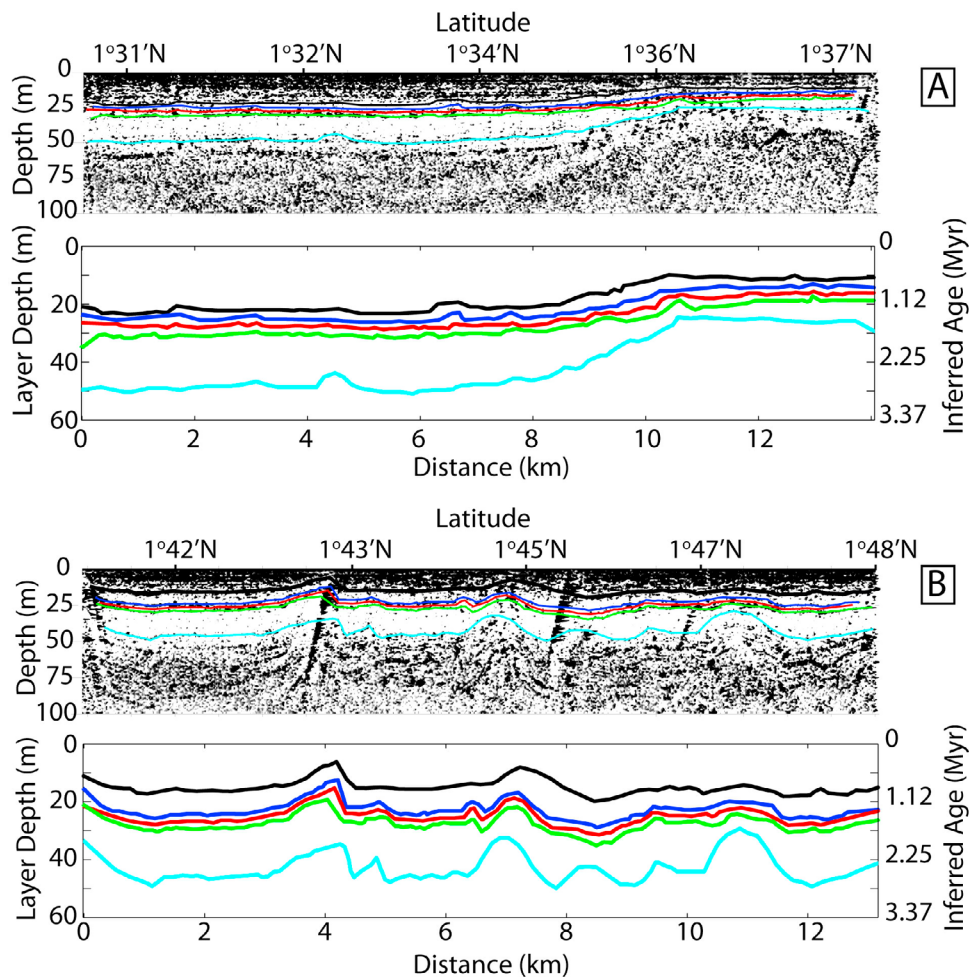
Figure 3. Sub-bottom chirp data collected to the (a) north and (b) south of a former ridge axis. These data were gathered during a sub-bottom transect along a nearly N–S oriented ship track located at ~90.5°W. Two-way travel time is converted to depth beneath the seafloor by assuming sound speeds that vary between 1500 and 1800 m s^{-1} within the first 150 m of seafloor. Significant reflections are digitized (colored lines) and converted to an inferred age of sedimentation on the basis of sedimentation rates determined at ODP site 851 [*Pisias et al.*, 1995].

[25] The volume of each lineament is dominated by several large volcanoes. The large seamounts are composite volcanoes, made up of numerous smaller cones (n = 93, Figure 5) suggesting relatively fixed and well-established melt extraction pathways at these locations. This may reflect a positive feedback in dike focusing from the generation of a volcanic load on a thin rigid lithosphere [e.g., *Muller et al.*, 2001] and the development of these volcanoes over shorter time scales (i.e., without significant plate motion).

[26] Previous authors suggest that the elongations of seamounts in the NGVP are parallel to the lineaments' strike [*Harpp and Geist*, 2002; *Harpp et al.*, 2003; *Sinton et al.*, 2003; *Mittelstaedt and Ito*, 2005]. To quantify the lineament orientations,

we use a number of approaches (Figure 6). Following the work of *Sinton et al.* [2003], we first use linear regression to characterize lineament orientation. The regression is performed on the center-points of all identified seamounts in a given lineament. Results of these regressions are similar to those reported in *Sinton et al.* [2003], with the linear fits to the lineaments intersecting near 0–1°N and 90.5–91°W. Near the ridge axis, the strike of each lineament changes to meet the ridge axis at a nearly right angle suggesting that the lineaments actually have arcuate shapes. However, the improvement in the correlation coefficient when using second order polynomials is small (Table 3).

[27] Within the NGVP, the degree of elongation of individual seamounts (i.e., aspect ratio) does not
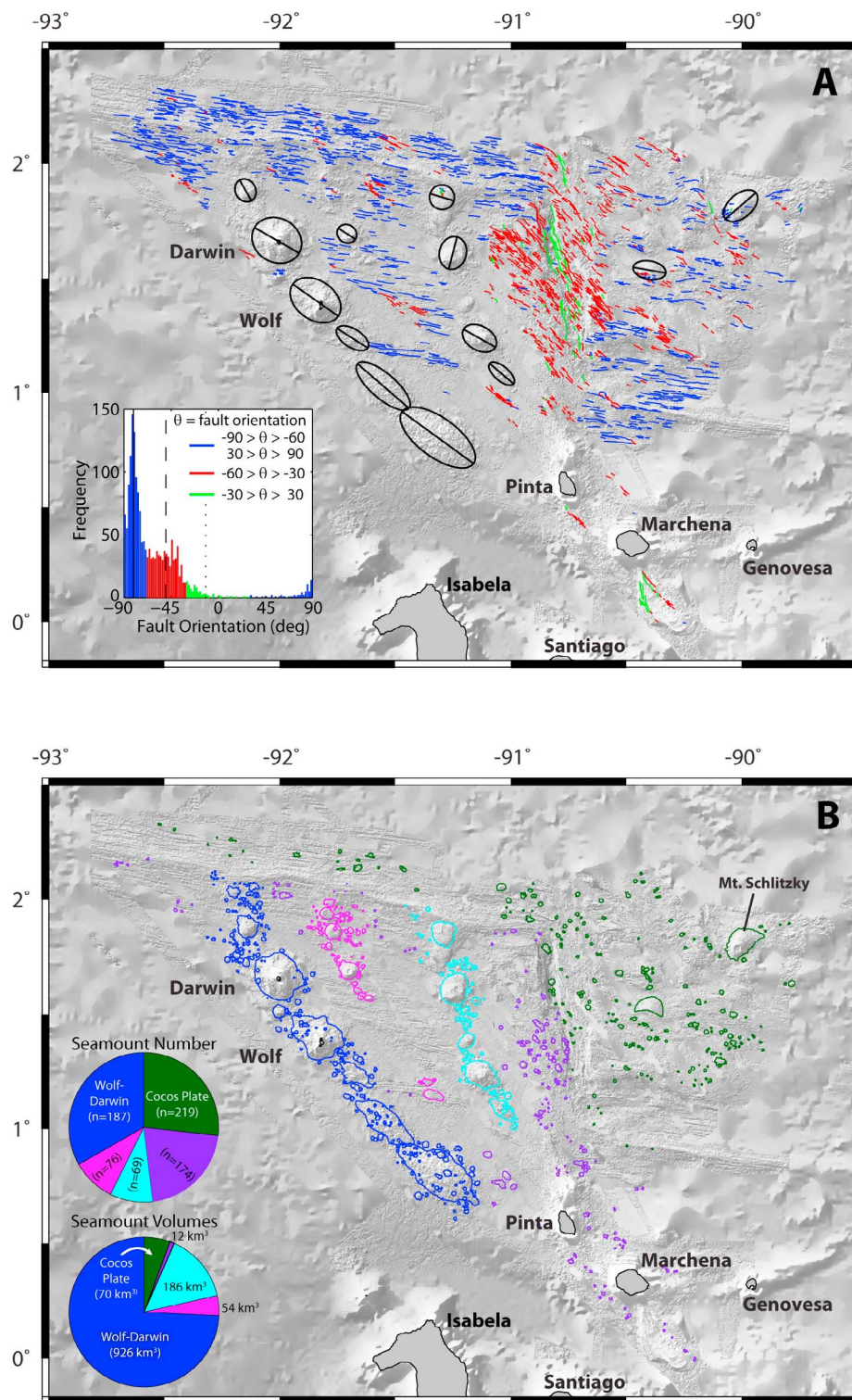
Figure 4. (a) The >1700 observed faults are placed into 3 groups based upon their orientation: (1) ridge parallel (blue), (2) transform-parallel (green), and (3) transform oblique (red). The directions of elongation of the largest seamounts along the Galápagos lineaments (black ovals) are primarily sub-parallel to this third fault group. Faults are identified using both side scan reflectivity and bathymetry data. (b) Primarily using the bathymetry data, we identify 818 individual seamounts with a combined volume of 1254 km^3. Approximately 73% of the seamounts in our study area are found on the Nazca Plate, this number includes 94% of the measured erupted volume suggesting a different melting regime beneath the Cocos Plate.

Table 2. Seamount Volumes

Seamount Group	Number	Volume (km^3)
All	725	1248
East of GTF (all)	219	70
West of GTF (all)	506	1178
Wolf-Darwin Lineament	187	926
Central Lineament	76	54
Eastern Lineament	69	186
West of GTF, non lineament	174	12

vary systematically with seamount size, but we find that the largest seamounts exhibit the most uniform orientation of their long-axes at ∼300° (Figure 4a). However, it is important to note that many seamounts are not elongate and many are elongate in random orientations. The degree of elongation in the largest seamounts is least near the ridge axis. In contrast to conclusions drawn in several previous studies [*Harpp and Geist*, 2002; *Harpp et al.*, 2003; *Mittelstaedt and Ito*, 2005], however, the elongation of the seamounts is not parallel to the lineament strikes determined above.

3.2. Fault Orientation and Length

[28] The pattern of faulting in the NGVP provides important insight into the distribution of regional
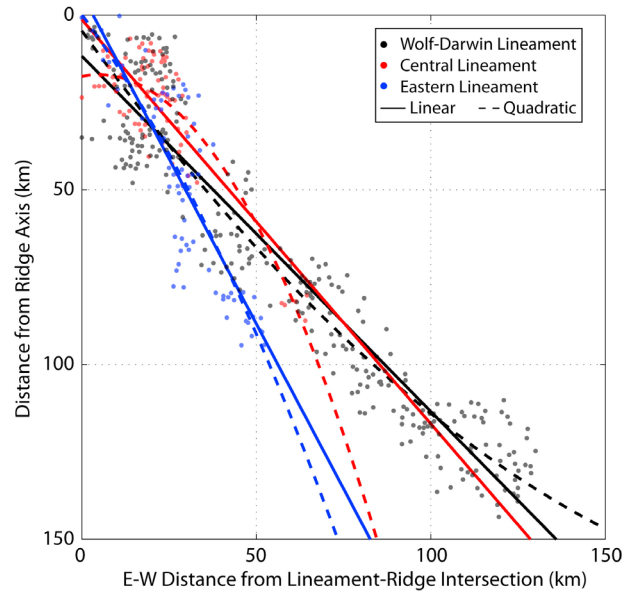

Figure 6. Lineament orientations are determined by fitting both linear (solid lines) and quadratic (dashed lines) to the centers of the observed volcanoes within each lineament (colored dots). The origin of the fits is defined as the intersection of the lineaments with the GSC. The difference in the correlation coefficient between the linear and quadratic fits is negligible (Table 3).
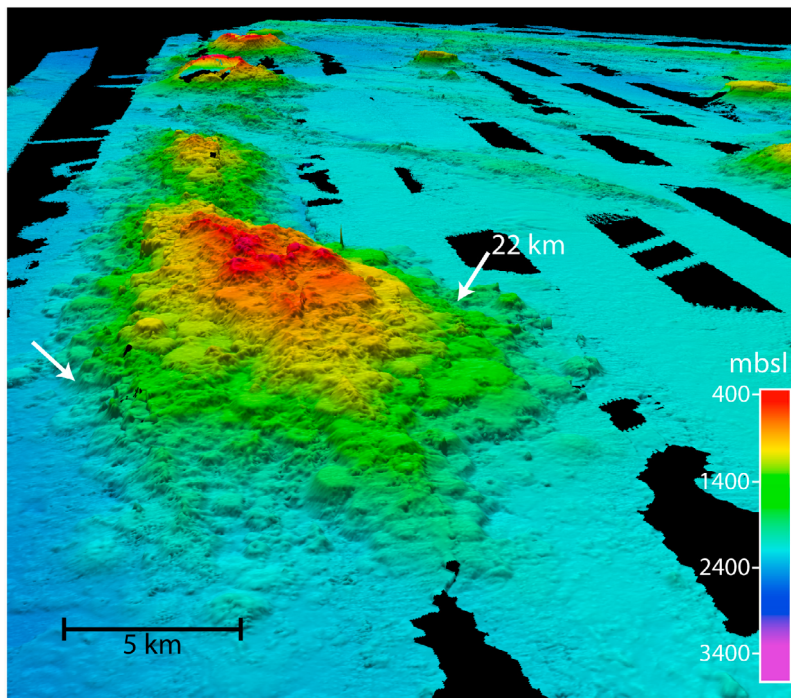

Figure 5. Although smaller seamounts appear to be formed from eruptions at a single vent, larger edifices are composite features with nascent rift zones and multiple vents. The 3D perspective view shows the southernmost volcano of the WDL and is oriented to the NW with a vertical exaggeration of 2. The distance between the white arrows is as indicated.

Table 3. Correlation Coefficients of Fits to Lineament Volcanoes

Lineament	R - linear	R - quadratic
Wolf-Darwin Lineament	0.954	0.959
Central Lineament	0.810	0.869
Easter Lineament	0.858	0.859

stresses as well as the timing of lineament formation. Over 1700 faults are identified within the survey area. The greatest concentrations of faults are near the ridge axes and the transform where fault densities are as high as 1 km/km^2 (i.e., 1 km of fault length per square km area). West of the GTF, fault density declines with increasing distance from the ridge axis, presumably due to burial by sediment. Faults are conspicuously absent in the vicinity of the seamount lineaments, which we attribute to coverage by lava flows and/or accommodation of strain by dikes rather than faults [*Rodgers et al.*, 1990].

[29] On the basis of their orientations and position, faults are categorized into three populations: ridge-parallel faults (270–290°), transform-parallel faults (338°–348°), and transform-oblique faults (290°–335°) (Figure 4). Ridge- and transform-parallel fault populations are consistent with gross seafloor morphology identified in some of the earliest regional studies of the GSC [e.g., *Johnson et al.*, 1976]. The transform-oblique fault population has not been previously described, but the presence of a transtensional regional stress field was predicted because of the oblique orientation of the GTF relative to both the ridge axes and the spreading direction [e.g., *Harpp and Geist*, 2002; *Harpp et al.*, 2003]. These faults are present in a ~60 km wide band centered on the transform fault, but fault densities are highest at the inside corners of the ridge-transform intersections as predicted by finite and boundary element models [e.g., *Fujita and Sleep*, 1978; *Gudmundsson*, 1995].

3.3. Sediments East of the Galápagos Transform Fault

[30] Sub-bottom chirp data were collected along a single N–S oriented transect from 0.75°N to 1.87°N at a longitude of approximately 90.5°W (Figure 2a), ~35 km to the east of the GTF, outside of the region of extensive transform-oblique faulting. Measured sediment thicknesses along this transect range from undetectable to a maximum of 65–70 m. Outside of the area near the ridge axis, no

attempt is made to interpret parts of the record where sediment thickness is indeterminate. Between the currently spreading ridge axis and 1.17°N (~27 km north of the axis), the seafloor is nearly devoid of sediments greater than ~3 m (our estimated detection limit). There is a sharp discontinuity in sediment thickness just north of this area where we measure the thickest sediment packages (~60 m) along the entire transect at ~1.17°N. Further to the north, sediment thickness steadily declines until it reaches a minimum (~20 m) at 1.46°N. Besides thin sediments (~5–28 m) atop a pair of small seamounts at ~1.66°N, sediment thickness increases from this minimum at 1.46°N until reaching ~50 m at 1.55°N, beyond which it remains approximately constant up to the northern limit of the transect at 1.87°N.

[31] Several of the identified sediment packages share similar characteristics, suggesting continuity between regions of accumulation separated by high-standing or tectonically disturbed terrains (Figure 3). In particular, two parts of the record at ~1.56°N and ~1.75°N have highly correlated sediment packages that consist of numerous shallow layers in the first ~10 m, a poorly reflective layer ~7–10 m thick, a distinctive pair of ~2–3 m thick sediment layers followed by another poorly reflective layer (~15–20 m thick), and finally a strong basement return. Locations at ~1.31°N and ~1.46°N also exhibit similar structures, but appear to be tectonically disturbed.

[32] We use sediment thicknesses along the N–S sub-bottom profile at 90.5°W as additional constraints on anomalous tectonics and ridge jumps east of the GTF. Sediment thicknesses in each location are converted to estimates of the approximate seafloor age using one of the nearest available sedimentation rates (~18 m Myr^{-1} since ~4 Ma) at site 851 from Ocean Drilling Project leg 138 at 2.77°N, 110°W [*Pisias et al.*, 1995]. This rate is slightly slower than that indicated by data from hole TR163–19 (~23 m Myr^{-1} since ~450 kyr) [*Lea et al.*, 2000], but the deeper core of *Pisias et al.* spans a larger age range more appropriate for this study. We avoid data from cores near the Galápagos Archipelago due to the high productivity of the islands (~100 m Myr^{-1}) [*Lea et al.*, 2006].

3.4. Magnetic Anomaly Profiles

[33] The locations of magnetic isochrons are chosen based upon the map of crustal magnetization. We evaluate the physical meaning of the isochron distribution by creating a series of synthetic anomaly
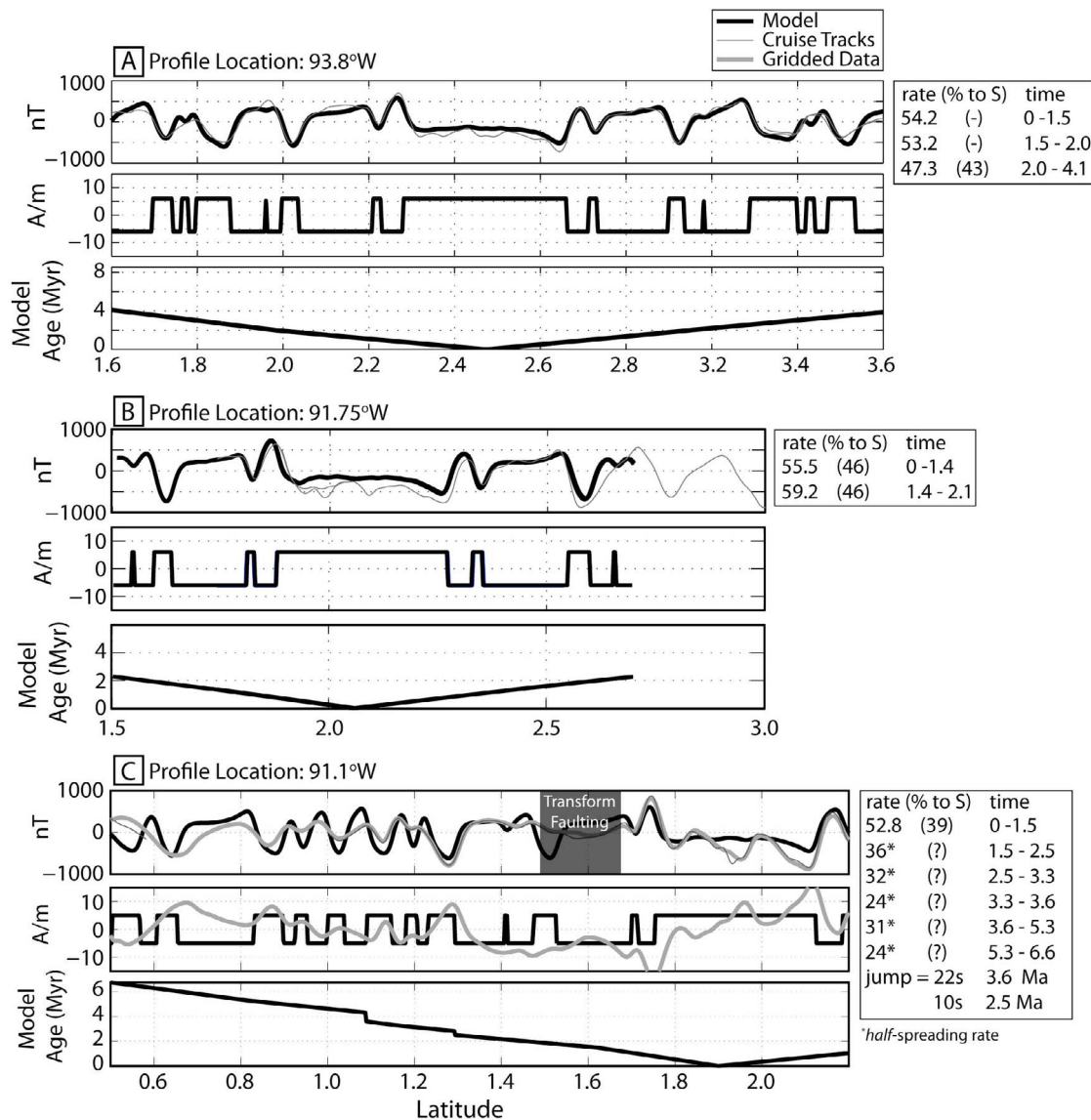
Figure 7. Synthetic models of magnetic anomaly profiles versus latitude (upper plots; thick, black lines) are created both west and east of the GTF by using an input age versus distance profile (lower plots, thick, black lines) to create a synthetic magnetization profile (middle plots; thick, black lines). Details of each model including full-spreading rate (km Myr^{-1}) and percent of that rate to the south (i.e., spreading asymmetry), periods of spreading (Ma), jump distances (km) and directions (s: south, n: north), and jump timings (Ma) are noted to the right of each plot. All models and interpolated profiles strike 10°E of N. Profiles at (a) 93.8°W and (b) 91.75°W are compared directly to older underway magnetic measurements (thin gray lines, Table 1) because these tracks fall either fully or partially outside of our study area. (c–f) Other profiles are also compared to underway data as well as to profiles interpolated from gridded magnetic data and the crustal magnetization solution (thick, gray lines). Estimated sediment deposition ages are plotted on the bottom plot of the profile located at 90.5°W. Anomalies are not interpreted in regions of anomalous volcanism or transform-oblique faulting that disrupts the magnetic anomaly pattern (dark boxes).

models along selected profiles (Figure 7). Each synthetic anomaly model is developed in a series of steps of increasing complexity. First, we attempt to fit the observed anomalies with symmetric spreading at rates previously published for the region

[*Wilson and Hey*, 1995]. In cases where the fit between model and observations is poor, we introduce changes to the spreading rate and asymmetry. If the model anomaly pattern still does not fit the observations, we introduce ridge jumps. The
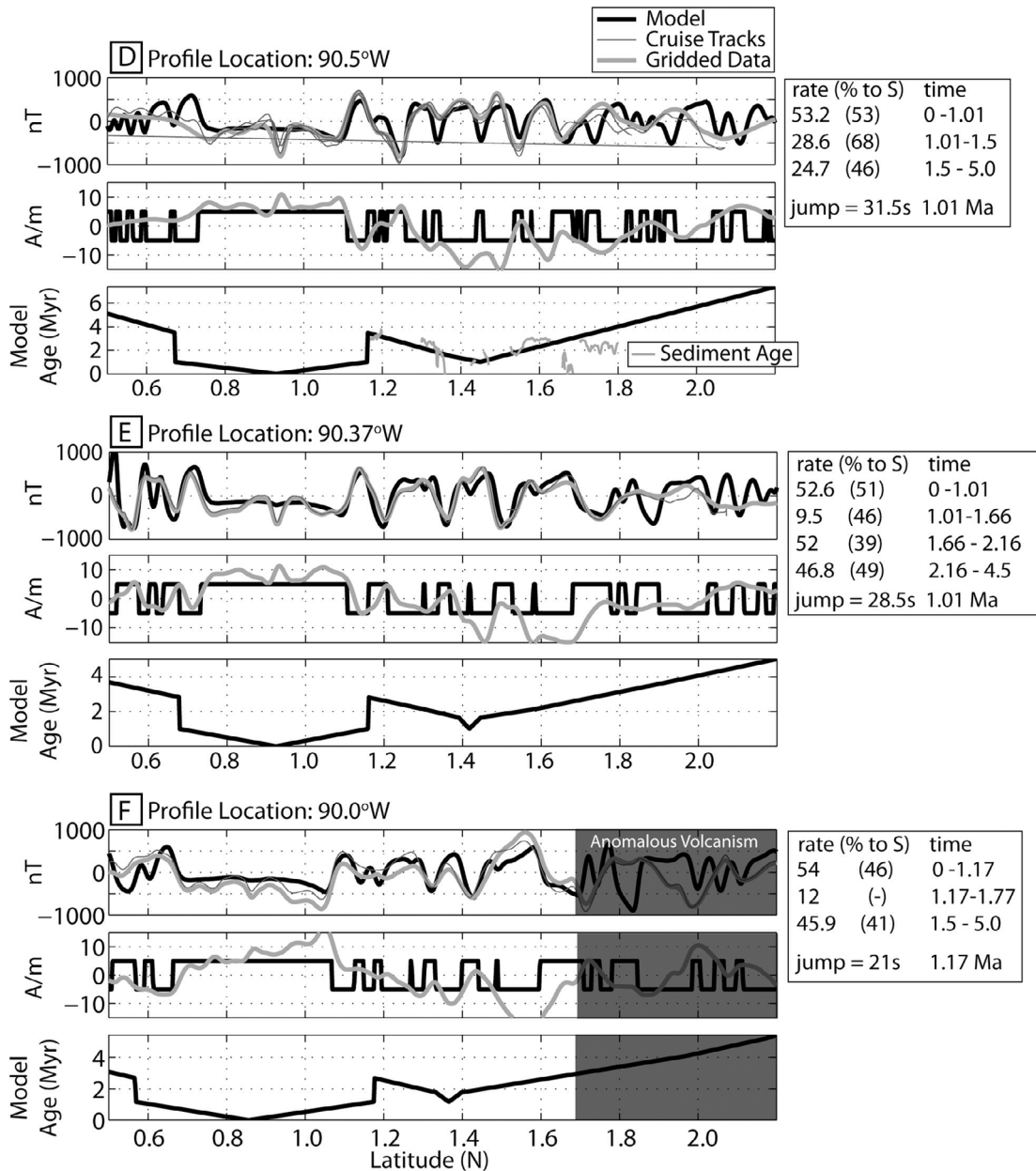
Figure 7. (continued)

location and timing of ridge jumps proposed herein are also constrained by bathymetry, sub-bottom chirp data, and fault maps. In all cases, we favor models with the simplest possible spreading history that still fit the available data.

[34] Anomalous faulting across a ∼60 km wide region around the GTF and several large seamounts disrupt the pattern of magnetic anomalies. We do not interpret or model magnetic anomalies in regions of strong tectonic or volcanic disruption.

3.4.1. Normal Spreading at 93.8°W

[35] An initial model is constructed in a region of normal spreading along the GSC. The model profile is projected along an azimuth of 5° and centered at 93.8°W (Figure 7a). The synthetic and observed anomalies closely coincide in both shape and polarity before ∼3.4 Ma (anomaly 2An.3n). Modeled full spreading rates are between 47.3 km Myr^{-1} and 54.2 km Myr^{-1} with nearly symmetric spreading from 2 Ma to present and asymmetric spreading 25% faster to the north before 2 Ma. The predicted

rates and asymmetry are similar to those of *Wilson and Hey* [1995] along a profile at 94.1°W. At ~3.4 Ma the anomaly pattern in this area no longer conforms to simple ridge spreading. *Wilson and Hey* [1995] predict a 7 km northward ridge jump at this time, but we do not attempt to interpret the profile beyond the limit of normal spreading as it is outside of our survey area. These modeled rates compare well with the geodetically determined 49.74 km Myr^{-1} [*Argus et al.*, 2011] and 53.65 km Myr^{-1} from a global circuit [*DeMets et al.*, 2010].

3.4.2. West of the Galápagos Transform Fault

[36] To the west of the GTF, we calculate two synthetic magnetic anomaly profiles oriented along an azimuth of 10° and located at 91.1°W and 91.75°W (Figures 7b and 7c). At 91.75°W, we compare the model results with ship tracks (not the gridded observations) from the 1979 Galápagos cruise of the R/V Kana Keoki, which include observations of the northern conjugate flank of the axis, allowing estimation of the full spreading rate (Figure 7b). The magnetic data from this ship track are best fit by slightly asymmetric spreading (slower to the south) at a full rate of 55.5 km Myr^{-1} until 1.4 Ma. From 1.4 Ma to 2.1 Ma, the spreading rate increases to 59.2 km Myr^{-1}. The profile located at 91.1°W is best fit by a full spreading rate of 52.8 km Myr^{-1} with slightly slower spreading to the south until 1.5 Ma. After 1.5 Ma, data are restricted to the Nazca plate and, because there is no data on the conjugate flank of the axis (i.e., the Cocos plate), we can only model half-spreading rates with unknown spreading asymmetries. From 1.5 Ma to 2.5 Ma, the best fit *half*-spreading rate (to the south) is 36 km Myr^{-1}. The ridge jumped ~10 km to the south at ~2.5 Ma, creating a pseudofault that is manifest as a change in faulting pattern traversing our study area. This pseudofault marks the passage of the 93.3°W overlapping spreading center that ceased propagation at ~0.4 Ma [*Wilson and Hey*, 1995; *Rotella et al.*, 2009]. Before this jump, the *half*-spreading rate was slightly slower at 32 km Myr^{-1} up to 3.3 Ma. Preceding this was a short period (~0.3 Ma) of slower spreading (24 km Myr^{-1}) following a ~22 km axis jump to the south at 3.6 Ma. This jump created a second, southern pseudofault that crosses our study area as a distinct faulting pattern (Figure 2). Prior to this jump, the *half*-spreading rate was ~31 km Myr^{-1} for ~2.7 Myr. Finally, from ~6.3 Ma to ~6.65 Ma the anomalies are best fit by a slower *half*-rate of 24 km Myr^{-1}.

3.4.3. East of the Galápagos Transform Fault

[37] East of the GTF, we calculate 3 synthetic magnetic anomaly profiles oriented at an azimuth of 10° and located at 90.5°W, 90.37°W, and 90.0°W (Figures 7d–7f). The westernmost profile, which is collocated with the sub-bottom chirp data (section 3.3, Figure 2a), is fit best by nearly symmetric spreading at a full-spreading rate of 53.2 km Myr^{-1} since ~1 Ma. Spreading along the present-day GSC was initiated at this time by a ~31.5 km southward ridge jump associated with westward propagation of the current axis. Before ~1 Ma, spreading was along a (now) fossil ridge axis at a full rate between 24.7 km Myr^{-1} and 28 km Myr^{-1}. Currently located at ~1.45°N (Figure 2), spreading along this former axis appears to have initiated near 3.0–3.5 Ma. The evolution of the ridge prior to ~3.0 Ma is poorly constrained owing to insufficient data coverage north and east of our study area. Consistent with this first profile, the best fit magnetic models at 90.37°W and 90.0°W include a jump from a (now) fossil spreading center to the current axis as it propagated westward.

3.5. The Pattern of Magnetization

[38] The crustal magnetization solution is used to aid in the location of magnetic anomalies throughout the study area, as summarized in Figure 8. Individual anomalies are identified along transects where synthetic models were calculated (section 3.4) by comparing the observed and modeled data. The location of a given isochron is defined as the location of the associated peak in magnetization magnitude or the location where the spatial derivative of the magnetization pattern taken perpendicular to the strike of the magnetic anomalies crosses zero, usually the center of each anomaly. Anomaly locations are picked along ship tracks only in regions without anomalous faulting and volcanism. Within the study area, we identify anomalies from 1n to 3An.1n (~6.1 Ma).

[39] Along the western GSC, the center of anomaly 1n does not follow the trace of the bathymetrically defined ridge axis everywhere. Anomaly 1n is centered ~10 km north of the axis for ~75 km to the west of the GTF. Beginning at the small overlapping spreading center located at 91.5°W the central anomaly and the axis more closely coincide. This pattern is well explained by an along axis gradient in spreading asymmetry since ~1.5 Ma; spreading is predicted to be slower to the south near the transform and nearly symmetric at 91.75°W. In contrast, along the eastern GSC, anomaly 1n is
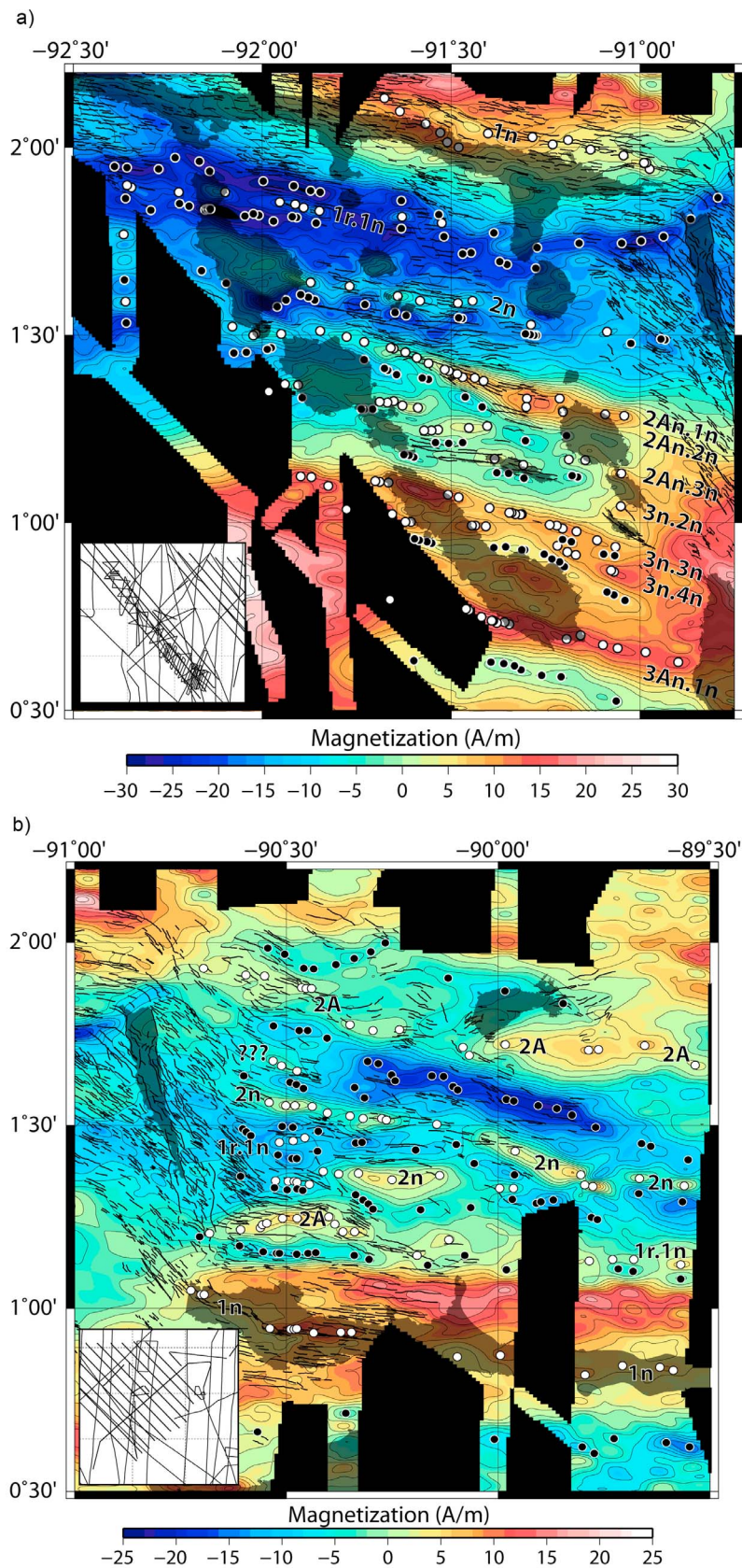
Figure 8

centered along the bathymetrically defined ridge axis throughout the study area reflecting nearly symmetric spreading since ~1 Ma.

[40] As previously noted for the Galápagos region [*Klitgord*, 1976; *Hey*, 1977; *Wilson and Hey*, 1995], we find that the crust is strongly magnetized in a predominantly linear pattern that is sub-parallel to the current ridge axes (Figure 8). The magnitude of magnetization does not steadily decrease with distance from the ridge axis as is often observed [*Irving*, 1970; *Macdonald and Luyendyk*, 1977; *Bleil and Petersen*, 1983], but instead exhibits peaks in magnetization for some anomalies away from the ridge axis. Several large volcanoes (e.g., the lineaments) and zones of post-spreading deformation disrupt the magnetization pattern. For example, the crustal magnetization within ~30 km west and east of the GTF is greatly reduced due to the extensive transform-oblique faulting (section 3.2). We do not interpret the magnetization pattern in these regions.

[41] Two strongly magnetized anomalies in the study area are of particular interest (Figure 8). The first is the positive anomaly 2An.1n located to the west of the GTF (~1.3°N, 91.1°W), which closely follows an anomalous faulting pattern that is oblique to the current spreading axis by 5°–9° (Figure 8a, section 3.2). The synthetic magnetic anomaly models predict this feature to be a pseudofault created by westward propagation of the 93.3°W overlapping spreading center. Second is a reverse polarity anomaly located east of the GTF (~1.6°N, 90.0°W), approximately parallel to a series of faults oblique to the current ridge axis. This anomaly strikes ~113.6° East of North, ~14° oblique to the current ridge axis. This strongly magnetized anomaly was formed at a modeled abandoned spreading center now located at ~1.45°N, but whether it is associated with a pseudofault is difficult to constrain due to insufficient data to the north. If the high magnetization does mark the initiation of spreading along this former

axis (i.e., a pseudofault), spreading would have initiated at ≥2.5 Ma.

3.6. Lava Differentiation Across the Northern Galápagos Volcanic Province

[42] Though not the focus of this work, variations in the lithologies of lavas dredged from the NGVP corroborate interpretations drawn from geophysical observations. Of the >40 successful dredges collected across the study area during the FLAMINGO cruise, all but 3 yielded lavas of basaltic compositions. West of the GTF, however, a glassy rhyolite was collected from the face of the southern pseudofault (D25; Figure 2a). East of the GTF, a dredge of lavas erupted near the pseudofault created by westward propagation of the current axis produced icelandites (D37), and a dredge on the fossil ridge (D39) included both icelandites and dacites. Similar compositions observed at mid-ocean ridges have been attributed to waning or low magma supplies associated with propagating ridge tips and overlapping spreading centers [e.g., *Fornari et al.*, 1983; *Perfit and Fornari*, 1983; *Christie and Sinton*, 1986; *Langmuir et al.*, 1986; *Sinton et al.*, 1991; *Wanless et al.*, 2010], where magmas experience more extensive differentiation than is commonly observed at mid-ocean ridges. High-magnitude magnetic anomalies throughout the study area may be due to concentrations of magnetite deposited in the crust by strongly fractionated magmas. A full description of the geochemical variations throughout the NGVP will be published elsewhere.

4. Discussion

4.1. The Galápagos Volcanic Lineaments

4.1.1. Observational Constraints on Lineament Formation

[43] The high density of normal faults near the GTF that strike ~30° oblique to its trace indicate that the GTF strongly perturbs the stress field of both the Cocos and Nazca plates. However, normal fault

Figure 8. (a) The pattern of crustal magnetization (filled, color contours) is predominantly linear and ridge-parallel. In several locations, however, the pattern is disturbed by anomalous volcanism (lineament volcanoes) and ridge-oblique faulting (black lines). We identify the center of magnetic anomalies (black numbers; white circles, normal polarity; black circles, reversed polarity) along ship tracks (map inset) that are outside of regions of anomalous volcanism and faulting. The dark gray regions are filled bathymetric contours delineating the ridge axis, transform, and lineament volcanoes. Regions without data coverage are masked (black areas). (b) Symbols and lines are identical to Figure 8a. The pattern of magnetization east of the transform fault exhibits a v-shaped pattern pointing to the east, strongly delineated by the high-magnitude reverse polarity anomaly between 2n and 2A, north of 1°30′N. Anomalies here were readily identified in all locations except between anomaly 2n and 2A near 90°30′W (question marks) which may have an anomalous magnetization associated with an overshoot of the western GSC axis.
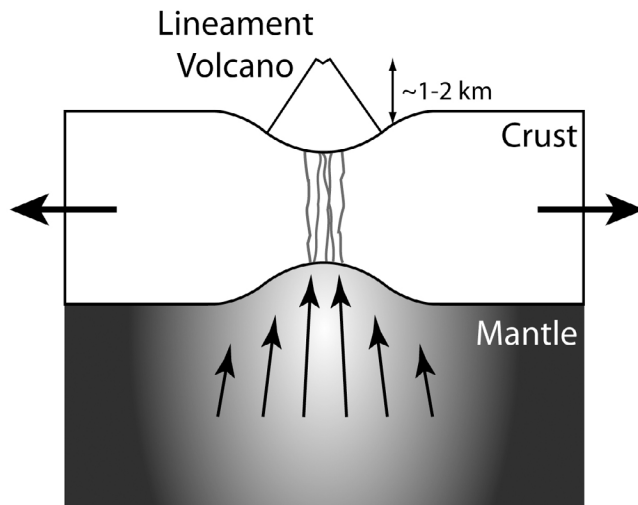
Figure 9. A conceptual model for decompression melting due to extension of the crust in the NGVP. Tension due to the oblique GTF causes extension and thinning of the crust beneath the Galápagos lineaments. As the crust thins, the underlying mantle rises in response and melts, potentially supplying the overlying lineament volcanoes.

orientations change sharply from oblique to approximately ridge-parallel beyond ∼30 km to the east or west of the transform trace, demonstrating decreasing influence of the GTF with distance, in agreement with Saint Venant's Principle [e.g., *Malvern*, 1969]. Although the Galápagos lineaments are located more than 30 km from the GTF, several of the large volcanoes that make up the lineaments are elongate in a direction roughly parallel to the orientation of the oblique faults near the GTF. The similar orientations of the seamount elongations and transform-oblique faults support the hypothesis that the stress field associated with the GTF influences the formation of individual volcanoes in the NGVP. However, the discrepancy between the volcano elongation orientations and the strike of the lineaments, as well as the decreasing seamount elongation toward the ridge axis, suggest that the GTF is not the sole factor controlling the regional-scale pattern of Galápagos lineaments. The decreasing elongation of larger volcanoes closer to the GSC may indicate an approximately isotropic near-ridge stress field, or alternately that those seamounts have not grown large enough to express the regional stress field.

4.1.2. Constraints on Lineament Formation From Geodynamic Modeling

[44] The volumes of the volcanic edifices that make up the Galápagos lineaments provide a primary constraint on their formation; complete models of lineament formation must include one or more mechanisms to produce at least this minimum volume of melt plus an unknown mass of complementary cumulates in the crust [*White et al.*, 2006]. Across-lineament extension is a possible mechanism to initiate upwelling and decompression melting of the underlying mantle [e.g., *Harpp and Geist*, 2002; *Harpp et al.*, 2003] (Figure 9). *Harpp and Geist* [2002] predicted such extension to occur at a rate of ∼8 mm yr^{-1} between the WDL and the GTF based upon the oblique strike of the GTF. Here, we use simple models of mantle flow and melting along with this predicted extension to evaluate whether uplift due to extension alone can produce sufficient melt to form the Galápagos lineaments.

[45] We solve the two-dimensional (2D) equations of conservation of momentum and mass for the instantaneous velocity field of an isoviscous mantle subject to a fixed rate of surface uplift (Figure 10, see Appendix A for model details). The model
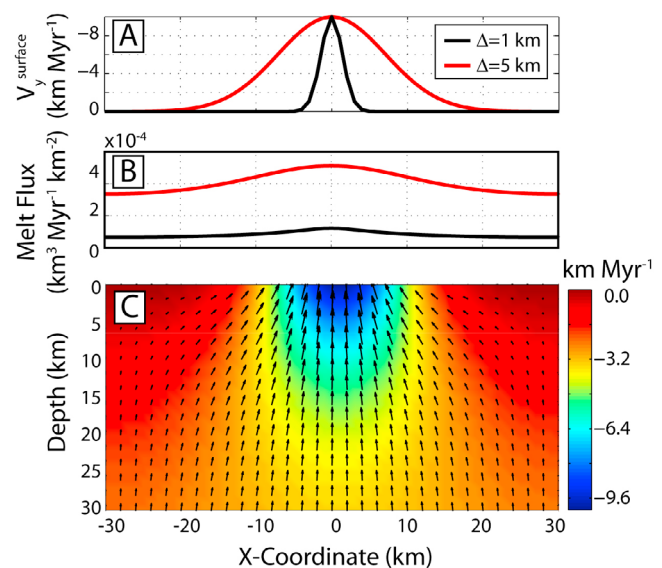

Figure 10. Instantaneous melting rate associated with extension-induced thinning of the crust (a possible source of lineament volcanism) is calculated by solving the equations of conservation of momentum and mass in a uniform viscosity mantle. (a) The surface boundary condition of the model for extension-induced melting is a Gaussian-shaped vertical velocity about the center of the domain. The standard deviation (Δ) of the Gaussian is either 1 km (black) or 5 km (red). The mantle responds to this surface condition by (c) upwelling (colors are vertical velocity and arrows are velocity vectors) and (b) melting due to decompression. Note that the velocity field in Figure 10c is for a case with Δ = 5 km.
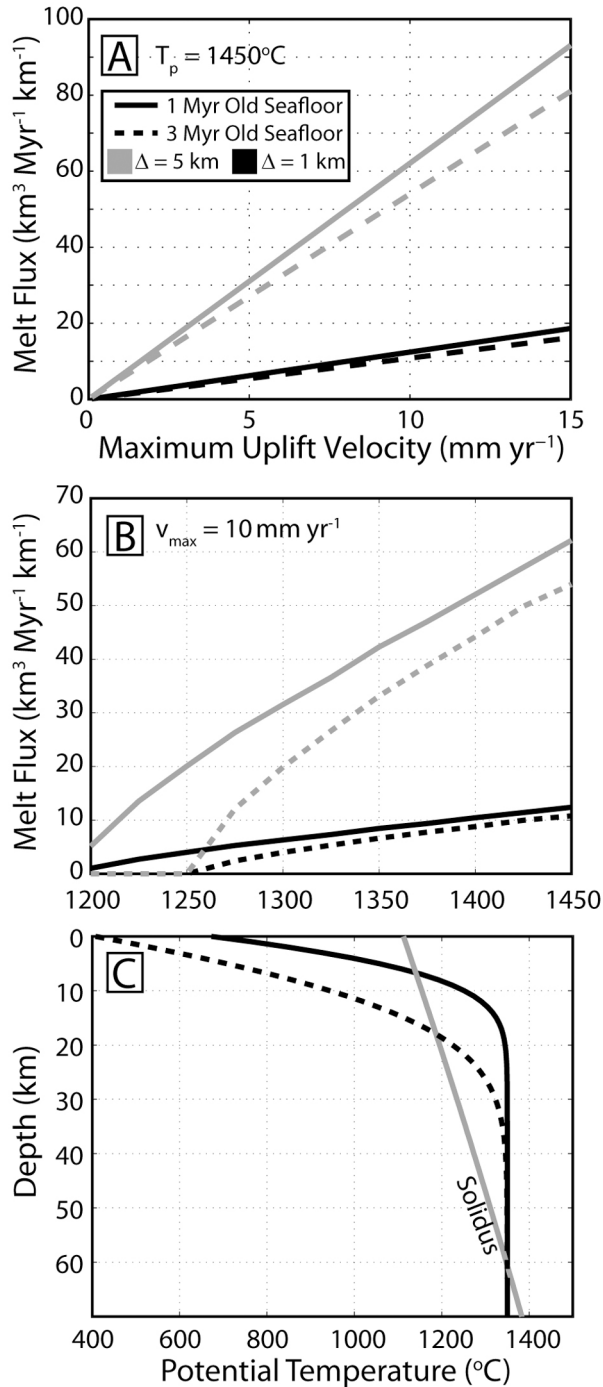
Figure 11. The integrated melt production rate per km along a lineament per million years of extension increases (a) linearly with maximum surface uplift rate and (b) asymptotically with the mantle potential temperature. In addition, the melt production rate is sensitive to (c) the thermal profile based upon a half-space cooling model with either 1 Myr old (solid lines) or 3 Myr old (dashed lines) seafloor ages. The solidus in Figure 11c is for dry peridotite from *Katz et al.* [2003]. The standard deviation of the width of surface uplift is either 1 km (black lines) or 5 km (gray lines).

domain is 60 km wide and 100 km deep and is assumed to be oriented perpendicular to the strike of a given lineament such that extension occurs parallel to the model domain. Thinning of the lithosphere by extension is not explicitly modeled. Instead, along the top surface of the model (assumed to correspond to the base of the crust) we prescribe a Gaussian vertical velocity profile with a maximum uplift rate v_{max} (varied between 0.1 mm yr^{-1} and 15 mm yr^{-1}) and a standard deviation Δ (set to either 1 km or 5 km). We impose a constant temperature structure corresponding to a half-space cooling model for a given seafloor age and a range of mantle potential temperatures (T_p = 1200°C–1450°C, Figure 11). Melt production rates (Figures 11a and 11b) are calculated by integrating the instantaneous melting rate (equation (B1)) within the model domain where the temperature is greater than the dry peridotite solidus of *Katz et al.* [2003]. Melt production rates are given in km^3 Myr^{-1} km^{-1}, the volume of melt created in 1 Myr per kilometer along the lineament. We artificially limit the width of mantle flow and melting by imposing a 60 km wide model domain to reflect a reasonable zone of melt accumulation [e.g., *Muller et al.*, 2001; *Ito and Martel*, 2002]. The models neglect the four following processes: (1) changes in mantle productivity with depletion (e.g., due to previous melting at the ridge axis); (2) stress- and temperature-dependent viscosity; (3) increased heat flux from the warm upper mantle as it rises toward the seafloor; and (4) cooling due to the latent heat of melting. Finally, we assume that all melt produced in the mantle reaches the seafloor. The above assumptions yield a maximum estimate of melt production, by which the effectiveness of cross-lineament extension as the source of lineament volcanism can be evaluated.

[46] The rate of melt production in the models varies with v_{max}, T_p, Δ, and the thickness of the overlying lithosphere or seafloor age (i.e., temperature gradient). Modeled melt production rates depend linearly on v_{max} with a slope that increases with increasing seafloor age and increasing width of the zone of uplift (Δ, Figure 11a). For example, a case with T_p = 1450°C, Δ = 1 km, and v_{max} = 5 mm yr^{-1}, yields a melt production rate of 6.2 km^3 Myr^{-1} km^{-1} that increases to 18.6 km^3 Myr^{-1} km^{-1} for v_{max} = 15 mm yr^{-1}. Raising potential temperature T_p leads to an asymptotic increase in the rate of melt production (Figure 11b). For an uplift rate of 10 mm yr^{-1} and a Δ = 5 km, melt production rates vary between ~5 km^3 Myr^{-1} km^{-1} and

$\sim$62 km^3 Myr^{-1} km^{-1} for potential temperatures between 1200°C and 1450°C. Increases in melt production with temperature approach an asymptote because each incremental rise in T_p causes a smaller fractional increase in the size of the melting zone.

[47] To determine whether decompression melting by extensional thinning of the lithosphere can create a volume of melt equivalent to the volume of the Galápagos lineaments, we require estimates of extension rate, duration of lineament volcanism, mantle potential temperature, and the age of the seafloor on which the lineaments erupted. Although not possible for all the lineaments, most of these variables can be constrained along the WDL: (1) ages of dredged lavas range from 0.1 Ma on the SE tip of the WDL to $\sim$1.8 Ma at Wolf Island [*White et al.*, 1993; *Sinton et al.*, 1996], (2) extension across the lineament is estimated to be up to 8 mm yr^{-1} [*Harpp and Geist*, 2002], (3) the excess temperature of the plume is predicted to decrease from $\sim$150°C beneath the archipelago to $\sim$30°C at the ridge axis [*Canales et al.*, 2002; *Hooft et al.*, 2003], and (4) seafloor age is $\sim$0–6 Myr based upon our magnetic anomaly identification.

[48] Consequently, to estimate the melt production rate due to extension along the WDL, we divide the WDL into 3 sections: the portion of the WDL on (1) 0–3 Myr old seafloor ($\sim$66 km long), (2) 3–5 Myr old seafloor ($\sim$54 km long), and (3) on 5–6 Myr old seafloor ($\sim$80 km long). For each section, the excess plume temperature above a 1315°C ambient mantle [*McKenzie et al.*, 2005; *Gibson and Geist*, 2010] is assumed to be a linear function of distance from Fernandina Island to the section center ($\Delta T_p = 39°C, 62°C, 83°C$), and the seafloor age is set to the mean age range for each section. For all 3 sections of the WDL, we assume that volcanic activity lasted at most $\sim$2 Myr, v_{max} is equal to 0.25 times the estimated 8 mm yr^{-1} extension rate (e.g., Poisson's ratio of 0.25 in a linear elastic plate), and $\Delta = 1$ km (uplift occurs across $\sim$6 km, similar to the lineament width). The standard deviation Δ is the least well constrained parameter in these models, but we choose a small value consistent with the lack of visible fractures parallel to the lineament volcanoes (i.e., any extensional deformation has been subsequently covered by volcanic activity). With these parameter values, the model predicts a melt production rate of $\sim$1.6 km^3 Myr^{-1} km^{-1}, $\sim$1.4 km^3 Myr^{-1} km^{-1}, and $\sim$1.5 km^3 Myr^{-1} km^{-1} for sections 1, 2, and 3 respectively, yielding a total integrated melt

production along the WDL of $\sim$594 km^3. This is $\sim$64% of the observed, extrusive volume of the WDL (924 km^3). To predict a total melt production equivalent to the observed WDL volume, extension must occur for >3 Myr, a number that is inconsistent with our magnetic reconstructions and the available age dates along the WDL.

[49] Melt production equivalent to the observed, extrusive WDL volume is also estimated for a uniform increase in T_p of >100°C for all three segments, or an upwelling rate >3.2 mm yr^{-1} (60% faster). Neither an increase in T_p nor a faster upwelling rate are consistent with other constraints; an increase of T_p by 100°C (maximum plume excess $T = 250°C$) disagrees with several estimates of plume temperature in the Galápagos [*Ito et al.*, 1997; *Hooft et al.*, 2003; *Putirka*, 2008; *Gibson and Geist*, 2010] although this is within the upper bounds of some of these studies, whereas an upwelling rate of 3.2 mm yr^{-1} is equivalent to 6.4 km of crustal thinning due to extension in 2 Myr, greater than the thickness of normal oceanic crust [*White et al.*, 1992]. Additionally, an unknown volume of intrusive lavas, commonly estimated to be equal to or greater than extrusive lavas [*White et al.*, 2006], must also be produced by this mechanism. Thus, other processes are needed to supply sufficient melt to produce the Galápagos lineaments. Three possible mechanisms include melting of plume material as it flows up the base of the thermal lithosphere, transport of melt from the region of plume melting beneath the Galápagos Archipelago, and/or plate driven upwelling near the axis.

[50] Flow of buoyant plume material up the base of the thermal lithosphere toward the ridge axis would result in uplift of the entire mantle column and a higher melt production rate than that predicted by extension-induced uplift. Such upwelling may be unlikely, however, owing to the predicted sharp increase of up to 2 orders of magnitude in mantle viscosities after water is removed during the initial stages of melting [*Hirth and Kohlstedt*, 1996]. This jump in mantle viscosity is predicted to produce a stiff compositional lithosphere with a base corresponding to the depth of the dry solidus [*Phipps Morgan*, 1997] and a slope much lower than what is predicted for a conductively cooled mechanical lithosphere. Plume material flowing beneath this stiff layer toward the ridge-axis is predicted to undergo only small degrees of melting [*Hall and Kincaid*, 2003] that would be volumetrically insignificant.

[51] Another potential source of eruptive material is melt from the plume stem that migrates along the top of the melting zone from the plume upwelling beneath the Galápagos Archipelago toward the ridge axis [e.g., *Sparks and Parmentier*, 1991; *Braun and Sohn*, 2003; *Hebert and Montési*, 2010]. At the top of the melting zone, an impermeable boundary is formed by freezing melt as it crosses the solidus. The remaining, buoyant melt collects in a high-porosity channel beneath this boundary and travels toward a local depth minimum (e.g., the ridge axis) where it accumulates and may erupt. As melt travels from the plume stem toward the ridge axis, it may collect along the base of the extensionally thinned parts of the plate and erupt through fractures prior to reaching the ridge axis. A compositional lithosphere would not prevent porous flow of melt through the mantle and so is consistent with this model. It is likely that only the lineament volcanoes closest to the plume stem may be supplied by this mechanism as uranium series disequilibria data require unrealistically rapid transport of melts from the plume to the GSC to match the plume signature observed along the ridge axis [*Kokfelt et al.*, 2005].

[52] Finally, plate-driven upwelling beneath the ridge axis and surrounding lithosphere could contribute to the volumes erupted at the Galápagos lineaments. The region of mantle upwelling that contributes to ridge-axis volcanism is at least several tens of kilometers wide [*Spiegelman and McKenzie*, 1987]. Melts produced by plate-driven upwelling will flow along the impermeable boundary just beneath the solidus. If the lineament volcanoes represent minima in the thermal boundary layer, melt may travel toward and accumulate at these locations. This could include melt that would have otherwise arrived at the ridge axis. We note that all of the above models require lithospheric thinning and/or development of fractures by tectonic extension to allow melt to accumulate beneath the solidus and reach the seafloor.

[53] To quantitatively evaluate the above mechanisms of melt supply to the lineaments, fully time-dependent models of mantle flow and melt transport are required. Such models are beyond the scope of the current work.

4.1.3. Evaluation of Models of Lineament Formation

[54] The first class of models for lineament formation on the Nazca Plate relies on asthenospheric channels or fingering of the plume to deliver excess plume material to the ridge axis where enhanced melting forms the volcanic lineaments [*Morgan*, 1978]. Experimental work shows that viscous fingers can develop aligned with the direction of plate motion in a low-viscosity material injected into a channel created by two parallel plates [*Weeraratne and Parmentier*, 2010]. The wavelength of these fingers scales as 12 times the channel thickness, which implies that if each lineament represents a viscous finger, the thickness of the fingering material beneath the Galápagos lineaments must be ∼2.5 km–4.2 km. If such fingers are present, they are too thin to be the buoyantly spreading plume material [e.g., *Delorey et al.*, 2007; *Villagómez et al.*, 2007], but could possibly be a thin layer of volatile rich or partially melted low-viscosity asthenosphere flowing beneath a rigid, depleted lithosphere [*Weeraratne and Parmentier*, 2010]. If such fingers do transport plume material to the axis, volcanic activity should reach a maximum at the lineament-ridge intersections. We do not, however, observe anomalous volcanic edifices in the bathymetric data, and there are no local peaks in seismically determined, near-axis crustal thickness [*Canales et al.*, 2002]. As originally formulated by *Morgan* [1978], this model also predicts an individual volcano within a lineament to have the same age as the seafloor upon which it sits, but $^{40}Ar/^{39}Ar$ dating of dredged samples from the WDL reveals volcanism >3 Myr younger than the surrounding seafloor [*White et al.*, 1993; *Sinton et al.*, 1996]. Also, there is no suggestion in the geochemistry of lavas from the WDL that plume material is flowing in a "mantle pipeline" toward the GSC [*Harpp and Geist*, 2002]. Specifically, this hypothesis predicts a strong plume signal that is progressively diluted to the northwest along the lineaments, which is not the case [*Harpp and Geist*, 2002].

[55] The second class of models suggests that the WDL is the surface expression of a lithospheric scale fault that forms a boundary between younger, weak lithosphere to the NE and older, stronger lithosphere to the SW [*Feighner and Richards*, 1994]. Although originally suggested as a mechanism for the formation of the WDL, it is unlikely that the other lineaments in the NGVP form by different processes, implying that there must be 3 lithospheric-scale faults west of the GTF. Such a large fault would require large stresses to develop in the plate, sufficient to surpass the yield strength of the entire lithosphere. Stresses of this magnitude are unlikely far from the ridge axis [*Mittelstaedt and Ito*, 2005], which suggests that such a fault would likely initiate at the axis, creating lineaments

with time progressive volcanism. Also, there is little to no evidence of any surface fracturing parallel to the WDL (Figure 4). Available dates along the WDL are consistent with northward and southward propagation of volcanism away from Wolf Island [*White et al.*, 1993; *Sinton et al.*, 1996], but geochronological data are not yet available along the other lineaments. The preferred gravity model used to develop this hypothesis [*Feighner and Richards*, 1994] introduces a sharp change in material properties across a fault that runs the length of the WDL and through the Galápagos platform, but recent ambient noise tomography suggests more gradual variations across the platform [*Villagómez et al.*, 2011].

[56] The final class of models propose that the location of magmatism in the NGVP is controlled by a lithospheric stress field perturbed by the nearby oblique transform fault and/or the upwelling plume impinging upon the base of the plate. The similar orientations of volcano elongations and the faults observed near the GTF (Figure 4) support the general hypothesis of stress control, but the discrepancy between these orientations and the shape of the lineaments (section 3.1) suggests that additional processes also influence the location of lineament volcanism. One such process could include additional perturbations to the regional stress field by the mantle plume [e.g., *Mittelstaedt and Ito*, 2005] and/or the ridge axis that may act as a shear-traction-free boundary. Also, the en echelon geometry of the lineament volcanoes along the WDL (Figure 4) may be indicative of Riedel-type deformation; deformation along the lineaments may include a left-lateral component. One curious observation is that there are no visible faults observed within the lineaments, possibly due to blanketing by recent volcanism or strain being accommodated by diking. The one exception to this is the saddle between Pinta and Marchena islands, where a series of NW-SE striking normal faults align approximately parallel to the long axis of Pinta Island (Figure 4). A difficulty with these models is that they do not successfully explain the volume of melt necessary to form the Galápagos lineaments (section 4.1.2).

[57] Our data and those of previous authors are most consistent with a model where the lithospheric stress field controls both faulting and the location of magmatism in the NGVP. The pattern of faults and seamount elongation indicate that the GTF and the ridge-axis boundary clearly contribute to the lithospheric stress field. It is difficult, however, to constrain whether plume spreading and buoyant uplift,

or other processes contribute to lineament formation. Further work, such as a teleseismic receiver function study similar to that performed at Hawaii [*Leahy et al.*, 2010], is needed to constrain these processes by imaging the structure of the crust and lithosphere beneath the Galápagos lineaments, and the extent of plume material spreading toward the GSC.

4.2. Jumps of the Galápagos Spreading Center

4.2.1. Two-Stage Formation of the Galápagos Transform Fault

[58] We propose a two-stage development of the GTF over ~2–3 Myr based upon several aspects of the GTF including the valley morphology, fault orientations, and the location of fossil ridges. In the north, the GTF is manifest as a deep pull-apart basin with transform-valley-parallel faults accommodating most of the deformation whereas, to the south, the transform valley is shallower and wider with both valley-parallel and valley-oblique faults accommodating deformation (Figure 4). The difference in faulting style is consistent with a younger age for the southern transform valley according to models that predict the development of transform faults in three principle stages: 1) an early stage of bookshelf faulting, followed by 2) the development of a Riedel-type distribution of faults, and finally 3) the establishment of a single transform fault trace [*Angelier et al.*, 2004, 2008]. In addition to a change in faulting style, the strike of the transform valley shifts by ~3.25° between the northern and southern valleys (Figure 2a). We also identify a fossil spreading ridge located at ~1.45°N, coincident with a minimum in sediment thickness (Figure 7d), a highly differentiated dredge sample (D39, Figure 2b), and a v-shaped crustal magnetization pattern (Figure 8b). We propose that the jump to this now-abandoned axis established the initial transform offset of ~50–60 km and created the northern transform valley. A subsequent ~31.5 km southward ridge jump at ~1 Ma extended this initial offset and caused the formation of the southern transform valley (Figure 12).

4.2.2. The Evolution of the NGVP Since 5 Ma

[59] The previously unrecognized ridge jumps over the past 2 Myr that we propose change the history of NGVP over the past ~5 Myr (Figure 12). During this period, there have been at least 4 southward jumps of the ridge axis toward the plume. Of these
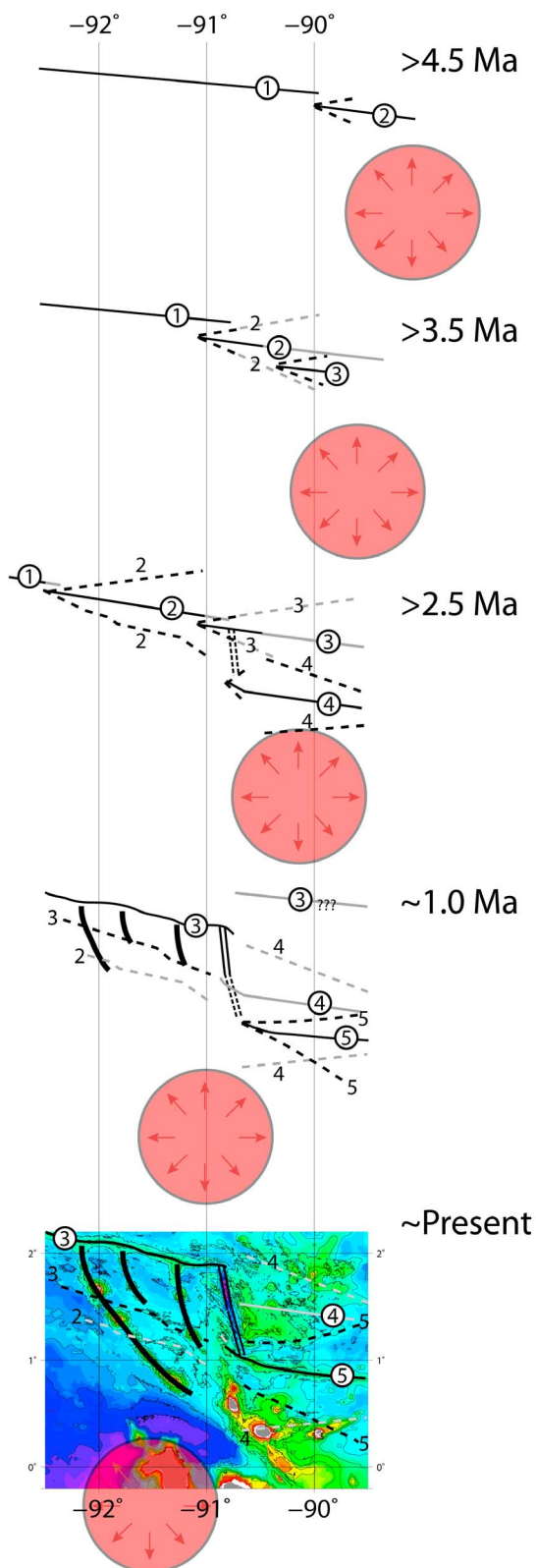
jumps, 3 appear to have established new axes that propagated away from the plume center with only the most recent jump initiating an axis that propagated toward the hot spot. Prior to ~4.5 Ma, a segment created by a southward ridge jump of ~20 km propagated westward, creating the southern pseudofault. As propagation of this segment continued, another southward jump of the axis toward the plume at ~3.5 Ma created a second westward propagating segment; this propagator recently ceased and formed the 93.3°W OSC. Sometime between 2.5 and 3.5 Ma, a third southward jump created an eastward propagating segment that offset the ridge axis by several tens of kilometers and formed the northern valley of the GTF. The establishment of the GTF created a trans-tensional stress field in both the Cocos and Nazca Plates similar to, but likely of smaller magnitude than that expressed today by the oblique faulting near the transform and the aligned elongation directions of large lineament seamounts. It is possible that eruptions along some of the lineaments began after creation of the northern transform valley. At ~1 Ma, the ridge again jumped southward by ~30 km as the currently spreading Eastern GSC propagated westward toward the GTF and the plume. This jump increased the offset between the Western and Eastern GSC and resulted in establishment of the southern valley of the GTF. The longer transform perturbed the lithospheric stress field further and promoted additional lineament volcanism likely including growth of the WDL, consistent with ^{40}Ar/^{39}Ar and K-Ar ages along the WDL that do not exceed 1.8 Ma [*White et al.*, 1993; *Sinton et al.*, 1996].

Figure 12. Tectonic reconstruction of the NGVP and the region east of the GTF (double lines, dashed or solid) based upon models of magnetic anomaly profiles, the pattern of crustal magnetization, sediment thicknesses, and seafloor morphology and faulting. The reconstruction is shown in the reference frame of the GTF with relative motion between the plume center (filled, pink circle) and the ridge axis (solid, black line) according to an estimated E–W motion of the Nazca Plate of 60 km Myr^{-1} [*Freymueller et al.*, 1993; *Trenkamp et al.*, 2002; *Sallarès and Charvis*, 2003; *O'Connor et al.*, 2007] and a northward motion of the GSC relative to the hot spot that is equal to the half-spreading rate [*Wilson and Hey*, 1995]. The lineaments (thick, black lines) are assumed to begin forming after the creation of both pseudofaults west of the GTF (dashed lines), which have since been overprinted by lavas. Each ridge segment (encircled numbers) and any associated pseudofaults (smaller numbers) in the reconstruction are numbered as they appear. Inactive ridges and pseudofaults are shown in gray. See the text for further details.

[60] Overall, the Galápagos plume dominated the evolution of the NGVP over the past several million years and, assuming a ridge migration rate equal to the half-spreading rate, the numerous southward jumps maintained a nearly fixed plume-ridge separation over the past ~5 Myr (145 km–215 km). The current plume-ridge separation distance is large (~180 km), but comparable to the separations we predict just prior to previous jumps of the axis, which may indicate that a new southward jump is imminent. If so, the currently active Marchena and Genovesa Islands are sites where weakened lithosphere may enable the development of a new ridge axis.

4.2.3. Comparison With Previous Reconstructions

[61] Previous studies examined the tectonic evolution of different sections of the GSC through modeling of observed magnetic anomaly profiles [*Anderson et al.*, 1975; *Klitgord*, 1976; *Hey*, 1977; *Wilson and Hey*, 1995]. We compare our new results (Figure 12) with those of the most recent study by *Wilson and Hey* [1995] (hereafter referred to as WH95), who integrated magnetic data from numerous cruises to reconstruct the spreading history along the GSC from 85°W to 96°W. The current study benefits from a range of constraints that were unavailable to WH95 including high-resolution multibeam bathymetry, side scan sonar reflectivity, a map of crustal magnetization, and sub-bottom chirp data.

[62] To the west of the GTF, our reconstruction differs in some details from WH95. South of the western GSC (~91°W, ~1°N), WH95 predict the existence of a single pseudofault initiated by a ~22 km southward ridge jump associated with westward propagation of the 93.3°W overlapping spreading center between ~3.5 Ma (at 91.1°W) and 0.4 Ma. The new bathymetry and side scan data reveal the presence of two pseudofaults west of the GTF (Figures 2 and 7). We interpret the northern pseudofault to reflect a ~10 km southward jump similar to that identified in WH95 related to propagation of the 93.3°W overlapping spreading center, but initiating at ~2.5 Ma (Figure 12). This ~1 Myr difference in the timing of propagator initiation suggests a propagation rate of ~110 mm/yr, ~40 mm/yr faster than predicted by WH95. We interpret the southern pseudofault to reflect a ~22 km southward jump at ~3.5 Ma at 91.1°W, but the fate of this propagator today is unclear. It is possible that the 93.3°W OSC overtook this earlier

propagator or that it merged with the original ridge axis.

[63] To the east of the GTF, between ~90.9°W and ~89.5°W, our reconstruction significantly differs from that of WH95. Since ~2 Ma, WH95 predict westward propagation of the current axis from 90.0°W to 90.8°W, which implies a propagation rate of 25 mm/yr, slower than the eastward migration rate of the entire GSC. In contrast, we predict westward propagation of the current axis from 90.0°W to 90.5°W between ~1.2 Ma and ~1 Ma at a propagation rate of 185 ± 15 mm/yr. An offset of ~80 km of anomaly 2A is interpreted by WH95 at 90.3°W, which they suggest formed through a series of ridge jumps responsible for creating the GTF. The high-resolution bathymetry maps and reflectivity data reveal that anomaly 2A is obscured in this region by a large, previously unmapped seamount centered at ~1.8°N, ~90.0°W and by faulting near the GTF. We interpret formation of the GTF in two parts with the northern valley initiating during or just before anomaly 2A and the southern valley initiating at ~1 Ma (section 4.2.1). Overall, our reconstruction supports WH95's interpretation of southward ridge jumps followed by propagation of new ridge segments keeping the GSC close to the Galápagos mantle plume.

[64] The timing and distance of the southward jumps of the GSC predicted in this study are consistent with scaling laws developed from numerical models of ridge jump formation [*Mittelstaedt et al.*, 2008, 2011]. In these models, jumps initiate as a result of thermal weakening of the off-axis lithosphere as magma passes through the plate. Such jumps are predicted to be more likely in younger, slower moving lithosphere. A compilation of observations from 7 hot spots around the world reveals that 11 out of 14 documented jumps occurred to seafloor ≤3 Myr old and during 13 out of these 14 jumps the half-spreading rates were <35 km Myr^{-1} [*Mittelstaedt et al.*, 2011]. In the current study, jumps occur to seafloor ≤1 Myr old at the time of the jump and for half-spreading rates between 25 km Myr^{-1} and 32 km Myr^{-1}.

4.3. Expressions of Plume-Ridge Interaction on the Cocos and Nazca Plates

4.3.1. Magmatism on the Cocos and Nazca Plates

[65] To the south of the GSC, on the Nazca Plate, there is voluminous off-axis volcanism in the NGVP, but to the north, on the Cocos Plate, there is

much less evidence of significant off-axis volcanism within ~100 km of the Eastern GSC. Extensive faulting bordering the GTF suggests that a similar stress field exists in the near-transform region of both the Cocos and Nazca Plates. Consequently, if comparable melt supplies (or geotherms) are present beneath the Cocos and Nazca Plates and the lithosphere is of approximately the same thickness, the pattern of volcanism should be similar on both sides of the transform fault. The lack of seamount volcanism east of the GTF therefore indicates that a change in melt supply must control the difference in volcanism between the Nazca and Cocos Plates. In other words, the volcanoes of the NGVP must result from *both* a stress field that promotes lineament volcanism and a higher melt supply on the archipelago side of the GSC.

[66] The larger amount of off-axis volcanism on the Nazca Plate is undoubtedly related to the Galápagos plume underlying that plate. Plume flow enhances magmatic productivity both by locally upwelling, as the plume material flows toward the GSC, and by increased melting due to the higher potential temperature of the plume. The GSC may be "capturing" most of the plume flow, or plume flow may change from upwelling beneath the archipelago and at the ridge-axis to horizontal or downward flow beneath the Cocos Plate. For example, melt may flow from the mantle region east of the GTF to the Western GSC and GTF itself, effectively stealing melt from beneath the Cocos Plate as the ridge migrates to the North [*Katz et al.*, 2004; *Hebert and Montési*, 2011].

4.3.2. Connections between Ridge Jumps and Volcanic Lineaments

[67] Recent ridge jumps and the formation of the volcanic lineaments in the Galápagos appear to be linked. Ridge jumps, at ~2.5–3.5 Ma and ~1 Ma, led to the two-stage formation of the GTF. This large offset of the GSC introduced large perturbations to the regional stress field that generated oblique faulting near the GTF and, possibly in conjunction with the nearby mantle plume, stress trajectories consistent with the volcanic lineaments. In addition to creating the GTF, post-jump ridge propagation formed numerous pseudofaults that likely acted as weak zones where magma preferentially erupted under the influence of the regional stress field. For example, our magnetic reconstructions place Pinta, Marchena, and Genovesa Islands near at least two pseudofaults (Figure 12). Magma

passing through the plate to form the lineament volcanoes heats and weakens the lithosphere, creating localized weak zones facilitating the formation of new ridge jumps [*Mittelstaedt et al.*, 2011]. As suggested in section 4.2.2, the islands of Marchena, and Genovesa may be in the process of weakening the off-axis lithosphere and initiating a new ridge jump as the plume and current axis continue to separate.

5. Conclusions

[68] We present observations and analysis of new multibeam bathymetry, side scan sonar, sub-bottom chirp, and total field magnetic data collected during the FLAMINGO cruise (MV1007, May–June 2010) to the Northern Galápagos Volcanic Province, the region of the Nazca Plate between the Galápagos Archipelago and the GSC, and to the region of the Cocos Plate east of the Galápagos Transform Fault. Within the study area, we observe extensive anomalous volcanism related to the nearby Galápagos hot spot, which has also dominated the tectonic evolution of the region.

[69] Bathymetry and side scan sonar data reveal significant variations in faulting and volcanism across the study area. Fault populations are placed into three categories: (1) ridge-parallel; (2) transform-parallel; and (3) transform oblique. Categories (1) and (2) are consistent with a standard model of mid-ocean ridge spreading. However, the third set of faults, located in a ~60 km wide swath around the Galápagos Transform Fault, strikes ~30° oblique to the trace of the transform and is not commonly observed at other transform faults. This orientation is likely associated with trans-tension across the GTF that is itself oblique to the ridge spreading direction.

[70] Volcanism in the study area is distinctly different between the Nazca and Cocos Plates and may indicate a sharp change in melting regime across the GSC. On the Cocos Plate to the north of the GSC, the observed number (219) and volume (70 km^3) of seamounts are small. In contrast, on the Nazca Plate to the south of the GSC, there are more than 500 identified seamounts with a total estimated volume of 1178 km^3. Seamount volcanism on the Nazca Plate is concentrated within 3 volcanic lineaments, the largest of which is the WDL. Within these lineaments, large, individual seamounts are generally elongate in a direction approximately parallel to the transform-oblique faulting, but the degree of elongation decreases toward the

ridge axis. This pattern suggests that the lithospheric stress field plays a role in the pattern of Galápagos lineaments.

[71] We use a numerical model of instantaneous mantle flow and melting rate to test whether extension-induced decompression melting can supply sufficient melt to produce the Galápagos lineaments. Assuming a set of parameters constrained for the WDL, the model results indicate that only ~60% of the measured volume of extrusive lavas can be produced by this mechanism; other sources of melt must have contributed to the construction of the Galápagos lineaments. Two alternative melt sources may include transport of melt from the plume stem along a high-porosity channel at the top of the melting zone, and decompression melting near the ridge axis caused by plate-driven upwelling.

[72] Magnetic anomaly modeling along with maps of crustal magnetization, sediment thicknesses, and seafloor morphology are used to reconstruct the tectonic history of the NGVP and the region east of the GTF. These data suggest numerous southward jumps of the ridge toward the hot spot across our study area. Since ~5 Ma, these jumps maintained a small but consistent plume-ridge separation of between ~145 km and ~215 km. East of the GTF, a southward jump at ~2.5–3.5 Ma resulted in formation of the northern pull-apart basin of the GTF. At ~1 Ma, the axis jumped ~31.5 km southward from the now extinct axis at ~1.45°N to the westward propagating axis of the currently spreading Eastern GSC. This jump extended the offset between the Western and Eastern GSC, resulting in formation of the southern valley of the GTF. West of the current location of the GTF, there were two southward ridge jumps of 22 km and 10 km at 3.6 Ma and 2.5 Ma, respectively. These jumps initiated propagating ridges, which created the two pseudofaults observed in the bathymetry and sonar data. Propagation of the current Western GSC, created by the more recent of these two jumps, ceased at the 93.3°W overlapping spreading center. Lineament seamounts overlie both pseudofaults suggesting a maximum age of initial volcanism along the Galápagos lineaments of ~2 Ma, consistent with current sparse geochronological data [*White et al.*, 1993; *Sinton et al.*, 1996].

[73] The tectonic history of the NGVP and the presence of the nearby Galápagos Plume are linked to the creation of the Galápagos lineaments. We propose that creation of the GTF was caused by southward ridge jumps associated with weakening of the near-ridge lithosphere by the plume. Formation of the GTF established a stress field favorable to magma penetration of the inside corner region of the Nazca Plate and melting of the Galápagos Plume supplied magma to construct the lineament volcanoes.

Appendix A: Mantle Flow Due to Localized Uplift

[74] To determine the instantaneous mantle flow field associated with localized uplift, we solve the 2D equations of conservation of mass and momentum for an incompressible, Boussinesq fluid

$$\nabla \cdot \mathbf{v} = 0 \tag{A1}$$

$$\nabla \cdot \left(\eta \left(\nabla \mathbf{v} + \nabla \mathbf{v}^T \right) \right) - \nabla P + \rho \mathbf{g} = 0 \tag{A2}$$

where $\mathbf{v}$ is the velocity (bold symbols denote vector quantities), η is the mantle viscosity, P is pressure, ρ is the density, and $\mathbf{g}$ is the acceleration of gravity (Table A1). The cross-sectional model domain measures 60 km laterally and 100 km vertically and is discretized into 60x100 nodal points. The velocity boundary conditions are free-slip on the vertical boundaries and a prescribed vertical velocity and zero lateral velocity on the horizontal boundaries. To conserve mass in the model, we impose identical inflow and outflow conditions along the bottom and top boundaries as $v_y = v_{max} \exp(-(x - x_{center})^2 / 4\Delta^2)$, where x and y are the horizontal and vertical coordinates, v_{max} is the maximum uplift rate at the center of the domain, and Δ is the standard deviation of the Gaussian function. Pressure boundary conditions include a zero horizontal pressure gradient at the model edges and zero pressure in one node along the surface boundary. To isolate the mantle flow field caused by the imposed vertical uplift rate along the top boundary, the bottom 5 km of the model domain are set to a constant, low viscosity (10^{16} Pa s), effectively decoupling this region from the rest of the model. The remainder of the domain has a constant viscosity (10^{19} Pa s), maximizing uplift and melt production in our model.

[75] Numerically, the equations are solved on a fully staggered grid using a primitive variable, finite difference formulation [e.g., *Gerya*, 2010] with solutions obtained in Matlab® by Gaussian elimination. The resulting instantaneous flow solution and a fixed temperature field equal to a half-space cooling model for a given seafloor age

Table A1. Modeling Parameters

Parameter	Description	Value	Units
c_p	Heat capacity of the mantle at constant pressure	1200	$J\,°C^{-1}\,kg^{-1}$
F	Melt fraction	-	-
g	Acceleration of gravity	9.81	$m\,s^{-2}$
$\dot{M}$	Melting rate	-	$m\,s^{-1}$
P	Pressure	-	Pa
ΔS	Entropy change, converting a solid to a liquid	200	$J\,°C^{-1}\,kg^{-1}$
T, T_p	Mantle potential temperature	-	$°C$
$T_{solidus}$	Temperature of mantle solidus	-	$°C$
v	Velocity of mantle flow	-	$m\,s^{-1}$
v_{max}	Maximum imposed uplift velocity	0.1–15	$mm\,yr^{-1}$
x, y	Horizontal and vertical spatial coordinates	-	m
α	Coefficient of thermal expansion	3.5×10^{-5}	$J\,°C^{-1}\,kg^{-1}$
Δ	Standard deviation of the Gaussian distribution of uplift	1, 5	km
η	Mantle viscosity	10^{19}	Pa s
ρ, ρ_{crust}	Mantle density, crustal density	3300, 2800	$kg\,m^3$

[*Turcotte and Schubert*, 2002] are then used to estimate the mantle melt production.

Appendix B: Calculation of the Rate of Mantle Melt Production

[76] The flux of melt from the mantle due to lithospheric uplift is calculated by depth integrating the productivity dF/dP multiplied by the rate of decompression

$$\dot{M} = -\int_{y_0}^{y_1} \left(\frac{dF}{dP}\right) \rho g v_y dy \qquad (B1)$$

where y_1 and y_0 are the bottom and top of the melting zone defined by the dry peridotite solidus of *Katz et al.* [2003], and $\dot{M}$ is the melt flux (per m^2) from the mantle. Following *Mittelstaedt et al.* [2011], the productivity is calculated where $T > T_{solidus}$ by assuming a constant change in entropy ($\Delta S = 200$ J kg^{-1} $°C^{-1}$) and a constant change in temperature with melt fraction dT/dF (570°C per percent F) from *Katz et al.* [2003, Figure 4]

$$-\frac{dF}{dP} = \frac{\left(\frac{\partial T}{\partial P}\right)_F - \frac{\alpha T}{\rho c_p}}{\left(\frac{\partial T}{\partial F}\right)_P + \frac{T\Delta S}{c_p}} \qquad (B2)$$

where α is the coefficient of thermal expansion, c_p is the heat capacity at constant pressure, and the pressure is defined as $P = \rho g y + \rho_{crust}\, g h_{crust}$ (see Table A1 for values) where $h_{crust} = 6$ km to account for the weight of a crustal layer atop the model domain. This formulation leads to mantle productivity changes that are only a function of temperature and pressure.

References

Anderson, R. N., D. A. Clague, K. D. Klitgord, M. Marshall, and R. K. Nishimori (1975), Magnetic and petrologic variations along the Galapagos Spreading Center and their relation to the Galapagos melting anomaly, *Geol. Soc. Am. Bull.*, *86*, 683–694, doi:10.1130/0016-7606(1975)86<683:MAPVAT>2.0.CO;2.

Angelier, J., R. Slunga, F. Bergerat, R. Stefansson, and C. Homberg (2004), Perturbation of stress and oceanic rift extension across transform faults shown by earthquake focal mechanisms in Iceland, *Earth Planet. Sci. Lett.*, *219*, 271–284, doi:10.1016/S0012-821X(03)00704-0.

Angelier, J., F. Bergerat, R. Stefansson, and M. Bellou (2008), Seismotectonics of a newly formed transform zone near a hotspot: Earthquake mechanisms and regional stress in the

South Iceland Seismic Zone, *Tectonophysics*, *447*(1–4), 95–116, doi:10.1016/j.tecto.2006.07.016.

Argus, D. R., R. G. Gordon, and C. DeMets (2011), Geologically current motion of 56 plates relative to the no-net-rotation reference frame, *Geochem. Geophys. Geosyst.*, *12*, Q11001, doi:10.1029/2011GC003751.

Batiza, R., and Y. Niu (1992), Petrology and magma chamber processes at the East Pacific Rise ∼9°30′N, *J. Geophys. Res.*, *97*(B5), 6779–6797, doi:10.1029/92JB00172.

Behn, M., J. M. Sinton, and R. S. Detrick (2004), Effect of the Galapagos hotspot on seafloor volcanism along the Galapagos Spreading Center (90.9–97.6°W), *Earth Planet. Sci. Lett.*, *217*(3–4), 331–347, doi:10.1016/S0012-821X(03)00611-3.

Blacic, T., G. Ito, J. P. Canales, R. S. Detrick, and J. M. Sinton (2004), Constructing the crust along the Galapagos Spreading Center 91.3° to 95.5°W: Correlation of seismic layer 2A with axial magma lens and topographic characteristics, *J. Geophys. Res.*, *109*, B10310, doi:10.1029/2004JB003066.

Blacic, T., G. Ito, A. K. Shah, J. P. Canales, and J. Lin (2008), Axial high topography and partial melt in the crust and mantle beneath the western Galapagos Spreading Center, *Geochem. Geophys. Geosyst.*, *9*, Q12005, doi:10.1029/2008GC002100.

Bleil, U., and N. Petersen (1983), Variations in magnetization intensity and low-temperature titanomagnetite oxidation of ocean floor basalts, *Nature*, *301*, 384–388, doi:10.1038/301384a0.

Bohnenstiehl, D., J. K. Howell, S. M. White, and R. N. Hey (2012), A modified basal outlining algorithm for identifying topographic highs from gridded elevation data, Part 1: Motivation and methods, *Comp. Geosci.*, doi:10.1016/j.cageo.2012.04.023, in press.

Braun, M. G., and R. A. Sohn (2003), Melt migration in plume-ridge systems, *Earth Planet. Sci. Lett.*, *213*, 417–430, doi:10.1016/S0012-821X(03)00279-6.

Canales, J. P., J. J. Danobeitia, R. S. Detrick, E. E. E. Hooft, R. Bartolome, and D. F. Naar (1997), Variations in axial morphology along the Galapagos spreading center and the influence of the Galapagos hot spot, *J. Geophys. Res.*, *102*(B12), 27,341–327,354, doi:10.1029/97JB01633.

Canales, J. P., G. Ito, R. S. Detrick, and C. W. Sinton (2002), Crustal thickness along the western Galapagos Spreading Center and the compensation of the Galapagos hotspot swell, *Earth Planet. Sci. Lett.*, *203*, 311–327, doi:10.1016/S0012-821X(02)00843-9.

Christie, D. M., and J. M. Sinton (1986), Major element constraints on melting, differentiation, and mixing of magmas from the Galapagos 95.5°W propagating rift system, *Contrib. Mineral. Petrol.*, *94*, 274–288, doi:10.1007/BF00371437.

Christie, D. M., R. Werner, F. Hauff, K. Hoernle, and B. B. Hanan (2005), Morphological and geochemical variations along the eastern Galapagos Spreading Center, *Geochem. Geophys. Geosyst.*, *6*, Q01006, doi:10.1029/2004GC000714.

Cushman, B., J. M. Sinton, and G. Ito (2004), Glass compositions, plume-ridge interaction, and hydrous melting along the Galapagos Spreading Center, 90.5°W to 98°W, *Geochem. Geophys. Geosyst.*, *5*, Q08E17, doi:10.1029/2004GC000709.

Delorey, A. A., R. Dunn, and J. B. Gaherty (2007), Surface wave tomography of the upper mantle beneath the Reykjanes Ridge with implications for ridge-hot spot interaction, *J. Geophys. Res.*, *112*, B08313, doi:10.1029/2006JB004785.

DeMets, C., L. I. Gordon, and D. R. Argus (2010), Geologically current plate motions, *Geophys. J. Int.*, *181*, 1–80, doi:10.1111/j.1365-246X.2009.04491.x.

Detrick, R. S., J. M. Sinton, G. Ito, J. P. Canales, M. Behn, T. Blacic, B. Cushman, J. E. Dixon, D. W. Graham, and J. Mahoney (2002), Correlated geophysical, geochemical and volcanological manifestations of plume-ridge interaction along the Galápagos Spreading Center, *Geochem. Geophys. Geosyst.*, *3*(10), 8501, doi:10.1029/2002GC000350.

Feighner, M. A., and M. A. Richards (1994), Lithospheric structure and compensation mechanisms of the Galapagos Archipelago, *J. Geophys. Res.*, *99*(B4), 6711–6729, doi:10.1029/93JB03360.

Fornari, D. J., M. R. Perfit, A. Malahoff, and R. W. Embley (1983), Geochemical studies of abyssal lavas recovered by DSRV Alvin from Eastern Galapagos Rift, Inca Transform, and Ecuador Rift: 1. Major element variations in natural glasses and spatial distribution of lavas, *J. Geophys. Res.*, *88*(B12), 10,519–10,529, doi:10.1029/JB088iB12p10519.

Freymueller, J. T., J. N. Kellogg, and V. Vega (1993), Plate motions in the North Andean region, *J. Geophys. Res.*, *98*(B12), 21,853–21,863, doi:10.1029/93JB00520.

Fujita, K., and N. Sleep (1978), Membrane stresses near mid-ocean ridge-transform intersections, *Tectonophysics*, *50*, 207–221, doi:10.1016/0040-1951(78)90136-1.

Garcia, S., N. Arnaud, J. Angelier, F. Bergerat, and C. Homberg (2003), Rift jump processes in Northern Iceland since 10 Ma from $^{40}Ar/^{39}Ar$ geochronology, *Earth Planet. Sci. Lett.*, *214*, 529–544, doi:10.1016/S0012-821X(03)00400-X.

Geist, D., B. A. Diefenbach, D. J. Fornari, M. D. Kurz, K. Harpp, and J. S. Blusztajn (2008), Construction of the Galápagos platform by large submarine volcanic terraces, *Geochem. Geophys. Geosyst.*, *9*, Q03015, doi:10.1029/2007GC001795.

Gerya, T. (2010), *Introduction to Numerical Geodynamic Modelling*, Cambridge Univ. Press, Cambridge, U. K.

Gibson, S. A., and D. Geist (2010), Geochemical and geophysical estimates of lithospheric thickness variation beneath the Galapagos, *Earth Planet. Sci. Lett.*, *300*, 275–286, doi:10.1016/j.epsl.2010.10.002.

Gradstein, F. M., J. G. Ogg, and A. G. Smith (2004), *A Geologic Time Scale*, Cambridge Univ. Press, U. K., doi:10.4095/215638.

Gudmundsson, A. (1995), Stress fields associated with oceanic transform faults, *Earth Planet. Sci. Lett.*, *136*, 603–614, doi:10.1016/0012-821X(95)00164-8.

Hall, P. S., and C. Kincaid (2003), Melting, dehydration and the dynamics of off-axis plume-ridge interaction, *Geochem. Geophys. Geosyst.*, *4*(9), 8510, doi:10.1029/2003GC000567.

Hardarson, B. S., J. G. Fitton, R. M. Ellam, and M. S. Pringle (1997), Rift relocation—A geochemical and geochronological investigation of a paleo-rift in northwest Iceland, *Earth Planet. Sci. Lett.*, *153*, 181–196, doi:10.1016/S0012-821X(97)00145-3.

Harpp, K., and D. Geist (2002), Wolf-Darwin lineament and plume-ridge interaction in northern Galapagos, *Geochem. Geophys. Geosyst.*, *3*(11), 8504, doi:10.1029/2002GC000370.

Harpp, K., and W. White (2001), Tracing a mantle plume: Isotopic and trace element variations of Galápagos seamounts, *Geochem. Geophys. Geosyst.*, *2*(6), 1042, doi:10.1029/2000GC000137.

Harpp, K., D. J. Fornari, D. Geist, and M. D. Kurz (2003), Genovesa Submarine Ridge: A manifestation of plume-ridge interaction in the northern Galápagos Islands, *Geochem. Geophys. Geosyst.*, *4*(9), 8511, doi:10.1029/2003GC000531.

Hebert, L. B., and L. G. J. Montési (2010), Generation of permeability barriers during melt extraction at mid-ocean ridges,

Geochem. Geophys. Geosyst., *11*, Q12008, doi:10.1029/2010GC003270.

Hebert, L. B., and L. G. J. Montési (2011), Melt extraction pathways at segmented oceanic ridges: Application to the East Pacific Rise at the Siqueiros transform, *Geophys. Res. Lett.*, *38*, L11306, doi:10.1029/2011GL047206.

Henkart, P. (1992), SIOSEIS–A computer system for enhancing and manipulating marine seismic reflection and refraction data, technical report, Scripps Inst. of Oceanogr., La Jolla, Calif.

Henkart, P. (2006), Chirp sub-bottom profiler processing–A review, *Sea Technol.*, *47*(10), 35–38.

Hey, R. N. (1977), Tectonic evolution of the Coco-Nazca spreading center, *Geol. Soc. Am. Bull.*, *88*, 1404–1420, doi:10.1130/0016-7606(1977)88<1404:TEOTCS>2.0.CO;2.

Hey, R. N., and P. R. Vogt (1977), Spreading center jumps and sub-axial asthenosphere flow near the Galapagos hotspot, *Tectonophysics*, *37*(1–3), 41–52, doi:10.1016/0040-1951(77)90038-5.

Hirth, G., and D. L. Kohlstedt (1996), Water in the oceanic upper mantle: Implications for rheology, melt extraction, and the evolution of the lithosphere, *Earth Planet. Sci. Lett.*, *144*(1–2), 93–108, doi:10.1016/0012-821X(96)00154-9.

Hooft, E. E. E., D. R. Toomey, and S. C. Solomon (2003), Anomalously thin transition zone beneath the Galapagos hotspot, *Earth Planet. Sci. Lett.*, *216*, 55–64, doi:10.1016/S0012-821X(03)00517-X.

Hsu, D. (1995), XCORR: A cross-over technique to adjust track data, *Comput. Geosci.*, *21*(2), 259–271, doi:10.1016/0098-3004(94)00070-B.

International Association of Geomagnetism and Aeronomy (2005), The 10th-generation international geomagnetic reference field, *Geophys. J. Int.*, *161*, 561–565, doi:10.1111/j.1365-246X.2005.02641.x.

Irving, E. (1970), The Mid-Atlantic Ridge at 45°N. XIV. Oxidation and magnetic properties of basalt; review and discussion, *Can. J. Earth Sci.*, *7*, 1528–1538, doi:10.1139/e70-144.

Ito, G., and J. Lin (1995), Oceanic spreading center-hotspot interactions: Constraints from along-isochron bathymetric and gravity anomalies, *Geology*, *23*, 657–660, doi:10.1130/0091-7613(1995)023<0657:OSCHIC>2.3.CO;2.

Ito, G., and S. J. Martel (2002), Focusing of magma in the upper mantle through dike interaction, *J. Geophys. Res.*, *107*(B10), 2223, doi:10.1029/2001JB000251.

Ito, G., J. Lin, and C. W. Gable (1997), Interaction of mantle plumes and migrating mid-ocean ridges: Implications for the Galapagos plume-ridge system, *J. Geophys. Res.*, *102*(B7), 15,403–15,417, doi:10.1029/97JB01049.

Ito, G., J. Lin, and D. Graham (2003), Observational and theoretical studies of the dynamics of mantle plume-mid-ocean ridge interaction, *Rev. Geophys.*, *41*(4), 1017, doi:10.1029/2002RG000117.

Johnson, G. L., P. R. Vogt, R. N. Hey, J. Campsie, and A. Lowrie (1976), Morphology and structure of the Galapagos Rise, *Mar. Geol.*, *21*, 81–120, doi:10.1016/0025-3227(76)90052-9.

Katz, R. F., M. Spiegelman, and C. H. Langmuir (2003), A new parameterization of hydrous mantle melting, *Geochem. Geophys. Geosyst.*, *4*(9), 1073, doi:10.1029/2002GC000433.

Katz, R. F., M. Spiegelman, and S. M. Carbotte (2004), Ridge migration, asthenospheric flow and the origin of magmatic segmentation in the global mid-ocean ridge system, *Geophys. Res. Lett.*, *31*, L15605, doi:10.1029/2004GL020388.

Klitgord, K. D. (1976), Sea-floor spreading: The central anomaly magnetization high, *Earth Planet. Sci. Lett.*, *29*, 201–209, doi:10.1016/0012-821X(76)90040-6.

Kokfelt, T. F., C. Lundstrom, K. Hoernle, F. Hauff, and R. Werner (2005), Plume–ridge interaction studied at the Galápagos spreading center: Evidence from ^{226}Ra–^{230}Th–^{238}U and ^{231}Pa–^{235}U isotopic disequilibria, *Earth Planet. Sci. Lett.*, *234*(1–2), 165–187, doi:10.1016/j.epsl.2005.02.031.

Kurz, M. D., and D. Geist (1999), Dynamics of the Galapagos hotspot from helium isotope geochemistry, *Geochim. Cosmochim. Acta*, *63*(23–24), 4139–4156, doi:10.1016/S0016-7037(99)00314-2.

Kurz, M. D., J. Curtice, D. J. Fornari, D. Geist, and M. Moreira (2009), Primitive neon from the center of the Galapagos hotspot, *Earth Planet. Sci. Lett.*, *286*, 23–34, doi:10.1016/j.epsl.2009.06.008.

Langmuir, C. H., J. F. Bender, and R. Batiza (1986), Petrological and tectonic segmentation of the East Pacific Rise, 5°30′–14°30′N, *Nature*, *322*(6078), 422–429, doi:10.1038/322422a0.

Lea, D. W., D. K. Pak, and H. J. Spero (2000), Climate impact of Late Quaternary equatorial Pacific sea surface temperature variations, *Science*, *289*, 1719–1724, doi:10.1126/science.289.5485.1719.

Lea, D. W., D. K. Pak, C. L. Belanger, H. J. Spero, M. A. Hall, and N. J. Shackleton (2006), Paleoclimate history of Galápagos surface waters over the last 135,000 yr, *Quat. Sci. Rev.*, *25*, 1152–1167, doi:10.1016/j.quascirev.2005.11.010.

Leahy, G. M., J. A. Collins, C. Wolfe, G. Laske, and S. C. Solomon (2010), Underplating of the Hawaiian swell: Evidence from teleseismic receiver functions, *Geophys. J. Int.*, *183*, 313–329, doi:10.1111/j.1365-246X.2010.04720.x.

Macdonald, K. C., and B. P. Luyendyk (1977), Deep-tow studies of the structure of the Mid-Atlantic Ridge crest near lat 37°N, *Geol. Soc. Am. Bull.*, *88*, 621–636, doi:10.1130/0016-7606(1977)88<621:DSOTSO>2.0.CO;2.

Macdonald, K. C., S. P. Miller, S. P. Huestis, and F. N. Spiess (1980), Three-dimensional modeling of a magnetic reversal boundary from inversion of deep-tow measurements, *J. Geophys. Res.*, *85*(B7), 3670–3680, doi:10.1029/JB085iB07p03670.

Maia, M., et al. (2011), Building of the Amsterdam-Saint Paul plateau: A 10 Myr history of a ridge-hot spot interaction and variations in the strength of the hot spot source, *J. Geophys. Res.*, *116*, B09104, doi:10.1029/2010JB007768.

Malvern, L. E. (1969), *Introduction to the Mechanics of a Continuous Medium*, Prentice-Hall, London.

McKenzie, D., J. Jackson, and K. F. Priestley (2005), Thermal structure of oceanic and continental lithosphere, *Earth Planet. Sci. Lett.*, *233*, 337–349, doi:10.1016/j.epsl.2005.02.005.

Meschede, M., and U. Barckhausen (2000), Plate tectonic evolution of the Cocos-Nazca Spreading Center, *Proc. Ocean Drill. Program Sci. Results*, *170*, 10 pp.

Mittelstaedt, E., and G. Ito (2005), Plume-ridge interaction, lithospheric stresses, and the origin of near-ridge volcanic lineaments, *Geochem. Geophys. Geosyst.*, *6*, Q06002, doi:10.1029/2004GC000860.

Mittelstaedt, E., G. Ito, and M. Behn (2008), Mid-ocean ridge jumps associated with hotspot magmatism, *Earth Planet. Sci. Lett.*, *266*(3–4), 256–270, doi:10.1016/j.epsl.2007.1010.1055.

Mittelstaedt, E., G. Ito, and J. van Hunen (2011), Repeated ridge jumps associated with plume-ridge interaction, melt

transport, and ridge migration, *J. Geophys. Res.*, *116*, B01102, doi:10.1029/2010JB007504.

Morgan, W. J. (1978), Rodriguez, Darwin, Amsterdam: A second type of hotspot island, *J. Geophys. Res.*, *83*(B11), 5355–5360, doi:10.1029/JB083iB11p05355.

Muller, J. R., G. Ito, and S. J. Martel (2001), Effects of volcano loading on dike propagation in an elastic half-space, *J. Geophys. Res.*, *106*(B6), 11,101–11,113, doi:10.1029/2000JB900461.

O'Connor, J. M., P. Stoffers, J. R. Wijbrans, and T. J. Worthington (2007), Migration of widespread long-lived volcanism across the Galapagos Volcanic Province: Evidence for a broad hotspot melting anomaly?, *Earth Planet. Sci. Lett.*, *263*, 339–354, doi:10.1016/j.epsl.2007.09.007.

Parker, R. L., and S. P. Huestis (1974), The inversion of magnetic anomalies in the presence of topography, *J. Geophys. Res.*, *79*(11), 1587–1593, doi:10.1029/JB079i011p01587.

Perfit, M. R., and D. J. Fornari (1983), Geochemical studies of abyssal lavas recovered by DSRV Alvin from eastern Galapagos Rift, Inca Transform, and Ecuador Rift: 2. Phase chemistry and crystallization history, *J. Geophys. Res.*, *88*(B12), 10,530–10,550, doi:10.1029/JB088iB12p10530.

Phipps Morgan, J. (1997), The generation of a compositional lithosphere by mid-ocean ridge melting and its effect on subsequent off-axis hotspot upwelling and melting, *Earth Planet. Sci. Lett.*, *146*(1–2), 213–232, doi:10.1016/S0012-821X(96)00207-5.

Pisias, N., L. A. Mayer, and A. C. Mix (1995), Paleoceanography of the Eastern Equatorial Pacific during the Neogene: Synthesis of 128 drilling results, *Proc. Ocean Drill. Program Sci. Results*, *138*, 5–21, doi:10.2973/odp.proc.sr.138.101.1995.

Putirka, K. (2008), Excess temperatures at ocean islands: Implications for mantle layering and convection, *Geology*, *36*(4), 283–286, doi:10.1130/G24615A.1.

Rodgers, D. W., W. R. Hackett, and H. T. Ore (1990), Extension of the Yellowstone Plateau, eastern Snake River plain, and Owyhee Plateau, *Geology*, *18*(11), 1138–1141, doi:10.1130/0091-7613(1990)018<1138:EOTYPE>2.3.CO;2.

Rotella, M. D., J. M. Sinton, J. Mahoney, and W. I. Chazey (2009), Geochemical evidence for low magma supply and inactive propagation at the Galápagos 93.25°W overlapping spreading center, *Geochem. Geophys. Geosyst.*, *10*, Q09005, doi:10.1029/2009GC002445.

Sallarès, V., and P. Charvis (2003), Crustal thickness constraints on the geodynamic evolution of the Galapagos Volcanic Province, *Earth Planet. Sci. Lett.*, *214*, 545–559, doi:10.1016/S0012-821X(03)00373-X.

Schilling, J. G. (1991), Fluxes and excess temperatures of mantle plumes inferred from their interaction with migrating mid-ocean ridges, *Nature*, *352*, 397–403, doi:10.1038/352397a0.

Schilling, J. G., R. H. Kingsley, and J. D. Devine (1982), Galapagos hotspot-spreading center system: 1. Spatial petrological and geochemical variations (83°W–101°W), *J. Geophys. Res.*, *87*, 5593–5610, doi:10.1029/JB087iB07p05593.

Schilling, J.-G., D. Fontignie, J. Blichert-Toft, R. Kingsley, and U. Tomza (2003), Pb-Hf-Nd-Sr isotope variations along the Galápagos Spreading Center (101°–83°W): Constraints on the dispersal of the Galápagos mantle plume, *Geochem. Geophys. Geosyst.*, *4*(10), 8512, doi:10.1029/2002GC000495.

Sinton, J. M., S. M. Smaglik, J. Mahoney, and K. C. Macdonald (1991), Magmatic processes at superfast spreading mid-ocean ridges: Glass compositional variations along the East Pacific Rise 13°–23°S, *J. Geophys. Res.*, *96*(B4), 6133–6155, doi:10.1029/90JB02454.

Sinton, C. W., D. M. Christie, and R. A. Duncan (1996), Geochronology of Galapagos Seamounts, *J. Geophys. Res.*, *101*(B6), 13,689–13,700, doi:10.1029/96JB00642.

Sinton, J. M., R. S. Detrick, J. P. Canales, G. Ito, and M. Behn (2003), Morphology and segmentation of the western Galápagos Spreading Center, 90.5°–98°W: Plume-ridge interaction at an intermediate spreading ridge, *Geochem. Geophys. Geosyst.*, *4*(12), 8515, doi:10.1029/2003GC000609.

Small, C. (1995), Observations of ridge-hotspot interactions in the Southern Ocean, *J. Geophys. Res.*, *100*, 17,931–17,946, doi:10.1029/95JB01377.

Smith, D. K., and J. R. Cann (1992), The role of seamount volcanism in crustal construction at the Mid-Atlantic Ridge (24°–30°N), *J. Geophys. Res.*, *97*(B2), 1645–1658, doi:10.1029/91JB02507.

Smith, W. H. F., and D. T. Sandwell (1997), Global seafloor topography from satellite altimetry and ship depth soundings, *Science*, *277*, 1956–1962, doi:10.1126/science.277.5334.1956.

Sparks, D. W., and E. M. Parmentier (1991), Melt extraction from the mantle beneath spreading centers, *Earth Planet. Sci. Lett.*, *105*, 368–377, doi:10.1016/0012-821X(91)90178-K.

Spiegelman, M., and D. McKenzie (1987), Simple 2-D models for melt extraction at mid-oceans ridges and island arcs, *Earth Planet. Sci. Lett.*, *83*, 137–152, doi:10.1016/0012-821X(87)90057-4.

Taylor, B., K. Crook, and J. Sinton (1994), Extensional transform zones and oblique spreading centers, *J. Geophys. Res.*, *99*(B10), 19,707–19,718, doi:10.1029/94JB01662.

Toomey, D. R., E. E. E. Hooft, and R. S. Detrick (2001), Crustal thickness variations and internal structure of the Galapagos Archipelago, *Eos Trans. AGU*, *82*(47), Fall Meet. Suppl., Abstract T42B-0939.

Trenkamp, R., J. N. Kellogg, J. T. Freymueller, and H. P. Mora (2002), Wide plate margin deformation, southern Central America and northwestern South America, CASA GPS observations, *J. South Am. Earth Sci.*, *15*, 157–171, doi:10.1016/S0895-9811(02)00018-4.

Turcotte, D. L., and G. Schubert (2002), *Geodynamics*, 2nd ed., 456 pp., Cambridge Univ. Press, Cambridge, U. K.

Verma, S. P. (1983), Strontium and neodymium isotope geochemistry of igneous rocks from the North East Pacific and Gulf of California, *Chem. Geol.*, *41*, 339–356, doi:10.1016/S0009-2541(83)80028-X.

Verma, S. P., and J. G. Schilling (1982), Galapagos hot spot-spreading center system: 2. $^{87}SR/^{86}SR$ and large ion lithophile element variations (85°W–101°W), *J. Geophys. Res.*, *87*(B13), 10,838–10,856, doi:10.1029/JB087iB13p10838.

Villagómez, D., D. R. Toomey, E. E. E. Hooft, and S. C. Solomon (2007), Upper mantle structure beneath the Galapagos Archipelago from surface wave tomography, *J. Geophys. Res.*, *112*, B07303, doi:10.1029/2006JB004672.

Villagómez, D., D. R. Toomey, E. E. E. Hooft, and S. C. Solomon (2011), Crustal structure beneath the Galápagos Archipelago from ambient noise tomography and its implications for plume–lithosphere interactions, *J. Geophys. Res.*, *116*, B04310, doi:10.1029/2010JB007764.

Wanless, V. D., M. R. Perfit, W. I. Ridley, and E. M. Klein (2010), Dacite petrogenesis on mid-ocean ridges: Evidence for oceanic crustal melting and assimilation, *J. Petrol.*, *51*(12), 2377–2410, doi:10.1093/petrology/egq056.

Weeraratne, D. S., and E. M. Parmentier (2010), Astheno-spheric mantle flow by viscous fingering instabilities, Abstract DL11A-1821 presented at 2010 Fall Meeting, AGU, San Francisco, Calif., 13–17 Dec.

Wessel, P., and W. H. F. Smith (1991), Free software helps map and display data, *Eos Trans. AGU*, *72*, 441, doi:10.1029/90EO00319.

White, R., D. McKenzie, and K. O'Nions (1992), Oceanic crustal thickness from seismic measurements and rare earth element inversions, *J. Geophys. Res.*, *97*(B13), 19,683–19,715, doi:10.1029/92JB01749.

White, S. M., J. A. Crisp, and F. J. Spera (2006), Long-term volumetric eruption rates and magma budgets, *Geochem. Geophys. Geosyst.*, *7*, Q03010, doi:10.1029/2005GC001002.

White, W. M., A. R. McBirney, and R. A. Duncan (1993), Petrology and geochemistry of the Galapagos Islands: Portrait of a pathological mantle plume, *J. Geophys. Res.*, *98*(B11), 19,533–19,563, doi:10.1029/93JB02018.

Wilson, D. S., and R. N. Hey (1995), History of rift propaga-tion and magnetization intensity for the Cocos-Nazca spread-ing center, *J. Geophys. Res.*, *100*(B6), 10,041–10,056, doi:10.1029/95JB00762.